The stress heterogeneity effects on the heat build-up of semi-crystalline polymers: Theories and experiments

Lili Wan, Cristian Ovalle Rodas, Lucien Laiarinandrasana

The stress heterogeneity effects on the heat build-up of semi-crystalline polymers: Theories and experiments

L.Wan[1], C. Ovalle[1], L. Laiarinandrasana[1]

Mines Paris, PSL University, Centre des Matériaux, CNRS UMR 7633 BP 87, F-91003 Evry Cedex, France

Abstract

The heat build-up induced by the conversion of mechanical work into dissipative heat is a common and dangerous phenomenon on polymers subjected to static or dynamic loading. The temperature rise, linked to the strain rate and the local stress state, promotes the microstructural alteration and mechanical properties degradation. Therefore, without consideration of the temperature rise, the components lifetime may be over-estimated by the available prediction models.

In order to study the coupled heat build-up mechanisms and stress heterogeneity effects on semi-crystalline polymers, uniaxial tensile tests were carried out on two materials under different cross-head speeds on notched flat samples whose surface stress state is heterogeneous. During loading, the simultaneous sample surface temperature was recorded using high-accuracy infrared cameras. Image processing was applied to measure the sample geometry evolution, e.g. the notch root curvature radius. Besides, based on Bridgman theory, the analytical stress fields were computed.

A good correlation between mechanical responses, geometrical evolution, stress states and heat build-up was obtained regardless of the speed and material. The thermomechanical behavior during the load-softening is particularly remarkable due to the increase of stress triaxiality ratio. The inverted parabola heat build-up profile in thickness reveals a stress heterogeneity in plat sample thickness. The increasing cross-head speed leads to a higher temperature rise due to the heating regime transition from isotherm to adiabatic heating.

Further work will investigate the heat build-up and stress heterogeneity effects on pre-cracked specimens of higher stress triaxiality ratio. The development and numerical implementation of a fully-coupled 3D thermomechanical model, accounting for the heat build-up, will be an encouraging challenge.

1 Introduction

Polymers are extensively employed in various industries from automobile to aerospace sectors due to their high strength-to-weight ratio and easy processability. Understanding the mechanical behavior of polymers is therefore of prime importance. The stress-strain relationship of polymers has been studied analytically, experimentally and numerically by numerous authors [1, 2]. Polymer is a kind of rate and temperature sensitive material. The strain rate effects on yield [3, 4], strain softening and strain hardening [4], have been examined, as well as the temperature effects on the mechanical response [5]. As a highly dissipative material, the polymers under loading can generate a large amount of heat and result in a significant temperature rise, whose extent depends on the strain rate. This intrinsic heating phenomenon is known as heat build-up.

Different strain rates lead to a different heating regime, from adiabatic to isothermal heating (thermal conductivity approximates to zero or infinite). When the raised temperature approaches to the glass transition temperature Tg, the modification of materials microstructure and the degradation of mechanical properties may be accelerated.

In the thermomechanical transition regime, between isothermal and adiabatic heating, either metals or polymers can dissipate heat during loading. Taylor and Quinney [6] evaluated around 90% of plastic deformation converted into heat for metals, while Adams and Farris [7] found only 50% to 80% of deformation work conversion for Polycarbonate, the similar mechanical energy conversion percentage (45% to 85%) was confirmed by Rundnev [8] for a larger range of glassy semi-crystalline polymers and blends. The conversion fraction depends, in fact, on the strain and strain rate. The effects of the strain rate were first analyzed by Adam and Farris [7]. The strain and strain rate dependencies were studied later by Rittel [9, 10].

A significant temperature rise was measured experimentally by several authors for dynamic and cyclic loading. To name a few, Rittel [11] measured a temperature rise of 70 °C at the crack-tip of PMMA subjected to dynamic loading, Bellenger et *al.* [12] obtained more than 120 °C temperature elevation for the cyclic tests on fiber glass-reinforced polymers. The stress-softening, that commonly occurs for polymers under loading, was attributed to the increasing temperature rise [13] and the heat build-up accounts for one of the fracture cause in addition to the mechanical failure [14].

Besides, concerning modelling and simulation of mechanical responses of polymers, several constitutive models were developed and implemented in finite element codes. In the Boyce model [15],

the effects of temperature, strain, pressure, true strain softening and strain hardening were taken into account for glassy polymers under large inelastic deformation. A fully three-dimensional strain and temperature dependent model, implemented into a FE simulation code, was used to describe the large strain responses on PMMA [16]. Other numerical models can be seen in [17, 18, 19].

A thermo-elasto-viscoplasticity numerical model was developed by Basu et *al.* [20] for glassy polymers to study the stress and temperature fields ahead of the a blunted notch at several strain rates covering the adiabatic and isothermal regime. From the numerical results of [20], the concentrated plastic and heat zone locates at the crack tip under adiabatic condition, while a larger shear band and heating zone were obtained for the isothermal regime where the conductivity was considered. Shen et *al.* [21] takes into account the material damage in addition to the thermo-elastic-viscoplastic consititutive behavior, aiming at describing the thermomechanical responses of thermoplastics at finite deformation. The model was then implemented in an element finite code to reproduce the heat build-up for flat smooth samples under uniaxial tensile loading, a good agreement was obtained between experimental and numerical surface temperature fields. Another thermo-viscoelastic model was implemented in Abaqus by Maximilian et *al.* [22] in taking into account the heat dissipation for fiber-reinforced polymer composite under cyclic loading.

The concentration of heating zone around the crack-tip reveals that the heat build-up is strongly related to the stress state, but few studies investigate the stress gradient and triaxiality effects on the heat build-up, except Ovalle et *al.* [23]. In the work of [23], experimental methods were employed to investigate the stress triaxiality effects on the heat build-up using notched and pre-cracked samples at different strain rates, a numerical model was also used to reproduce the heat build-up under adiabatic condition, good agreements were found between experimental and numerical results.

To summarize, the heat build-up is a phenomenon exhibited by polymers during deformation, it can modify the mechanical response of the polymer. Moreover, if a significant heat build-up is attained, the mechanical properties of polymers can be degraded severely. Experimental tests were used to investigate the heat build-up under different loading types at various range of strain rate for different samples. A large range of constitutive models were developed and implemented in finite element codes aiming at reproducing and predicting the thermomechanical response of polymers in taking the temperature-dependent mechanical properties and the intrinsic heat dissipation into account. Nevertheless, a relation between the stress and the heat build-up fields haven't been explained while a strong correlation between them is revealed. Thus, the aim of this study is to find out the correlation between the theoretical stress field and the temperature distribution, as well as

the stress state effects on the heat build-up of polymers using theoretical and experimental methods. Two semi-crystalline polymers of different glass transition temperatures were investigated in this paper.

The theoretical stress state of flat notched samples based on the Bridgman theory will be introduced in Section 2. Uniaxial tensile tests were carried out on flat notched samples whose surface stress state is heterogeneous, the surface temperature was simultaneously measured by infrared cameras. The experimental protocol will be presented in Section 3. The mechanical and thermal results will be discussed in Section 4. This paper will then be closed by concluding remarks.

2 Stress fields on a notched sample

The round notched sample is a typical geometry used to study the effect of a multiaxial stress state on the materials mechanical response [24, 25, 26, 27]. Its stress state is heterogeneous along the minimum cross section radius, but circumstantially homogeneous. The flat notched samples, though, exhibit a stress heterogeneity through both width and thickness, it's therefore a better choice of for the study of the effects of a heterogeneous multiaxial stress state.

The stress fields of a flat notched sample at the minimum section were analytically developed by Bridgman [28] in assuming axisymmetric equivalence and plane strain hypotheses. For a notched flat sample (see figure 1a), with R the curvature radius at the notch root, their three principal stresses (σ_{xx}, σ_{yy}, σ_{zz}) and stress triaxiality ratio (τ_σ) are summarized in table 1. The net stress along the loading direction σ_{net}, ratio between the load F and the minimum cross section $2a*2t$, with a and t the mid-width and mid-thickness at the minimum cross section respectively, equals to:

$$\sigma_{net} = \frac{F}{2a * 2t} \tag{1}$$

The equivalent stress σ_{eq} equals to σ_{net} corrected by the geometrical dependent ratio a/R:

$$\sigma_{eq} = \frac{\sigma_{net}}{(1+2\frac{R}{a})log(1+\frac{a}{2R})} \tag{2}$$

Since 2D consideration, the stress state is homogeneous through thickness (y-axis). The real stress state, however, differs at least between the mid-thickness and the surface: the surface (y = $\pm$ t) is actually on plane stress condition with a null σ_{yy}, while the mid-thickness (y = 0) is under plane strain condition. To take such difference into account, plane stress hypothesis is therefore considered and completed by the authors based on Bridgman theory, see table 1. According to Bridgman, σ_{xx} and σ_{zz} are independent on the hypothesis, these two principal stresses are thus

Table 1: Stress fields for flat notched sample

	Axisymmetric Equivalence, Bridgman	Plane Strain, Bridgman	Plane Stress
σ_{xx}	$\sigma_{eq} log[1+\frac{a}{2R}(1-\frac{x^2}{a^2})]$	$\sigma_{eq} log[1+\frac{a}{2R}(1-\frac{x^2}{a^2})]$	$\sigma_{eq} log[1+\frac{a}{2R}(1-\frac{x^2}{a^2})]$
σ_{yy}	$\sigma_{eq} log[1+\frac{a}{2R}(1-\frac{x^2}{a^2})]$	$\sigma_{eq}\{\frac{1}{2}+log[1+\frac{a}{2R}(1-\frac{x^2}{a^2})]\}$	0
σ_{zz}	$\sigma_{eq}\{1+log[1+\frac{a}{2R}(1-\frac{x^2}{a^2})]\}$	$\sigma_{eq}\{1+log[1+\frac{a}{2R}(1-\frac{x^2}{a^2})]\}$	$\sigma_{eq}\{1+log[1+\frac{a}{2R}(1-\frac{x^2}{a^2})]\}$
τ_σ	$\frac{1}{3}+log[1+\frac{a}{2R}(1-\frac{x^2}{a^2})]$	$\frac{1}{2}+log[1+\frac{a}{2R}(1-\frac{x^2}{a^2})]$	$\frac{1}{3}+\frac{2}{3}log[1+\frac{a}{2R}(1-\frac{x^2}{a^2})]$

applied as well to plane stress hypothesis. With the knowledge of three principal stresses, the stress triaxiality ratio τ_σ under plane stress hypothesis can be determined by:

$$\tau_\sigma = \frac{\bar{\sigma}}{\sigma_{eq}} = \frac{(\sigma_{xx}+\sigma_{yy}+\sigma_{zz})/3}{\sigma_{eq}} = \frac{1}{3}+\frac{2}{3}log[1+\frac{a}{2R}(1-\frac{x^2}{a^2})] \tag{3}$$

where $\bar{\sigma}$ is the mean stress.

For a given load F and a/R, the spatial distributions of σ_{xx}, σ_{yy}, σ_{zz} and τ_σ along the sample width (x) at the notch root of three hypotheses were plotted respectively in figure 1b - 1e. Each parameter was normalized by their maximum value. The distributions display all an inverted parabola profile where the maximum value is located at the mid-width and decreases towards the notch root.

The σ_{xx} and σ_{zz} of three hypotheses superpose (figure 1b and 1d), the σ_{yy} is higher on plane strain than on axisymmetric equivalence (figure 1c). The τ_σ is highest on plane strain and lowest on plane stress (figure 1e), in other words, the τ_σ is more significant at mid-thickness (y = 0) than at the surface (y = $\pm$ t).

3 Methodology

3.1 Experimental procedure

3.1.1 Materials and Samples

Materials Two types of semi-crystalline polymers were investigated: a PolyEthylene (PE) and a PolyAmide 11 (PA11) supplied respectively by Technip and Arkema. Their physico-chemical properties are summarized in table 2. These two materials exhibits two different glass transition temperature Tg: the Tg of PE is -110 °C, while the one of PA11 is about 53 °C, respectively lower and higher than room temperature. The melting temperature of PA11 (188 °C) is higher than the one of PE (110 °C). PA11 has an index of crystallinity of about 20%. Both the crystallinity and

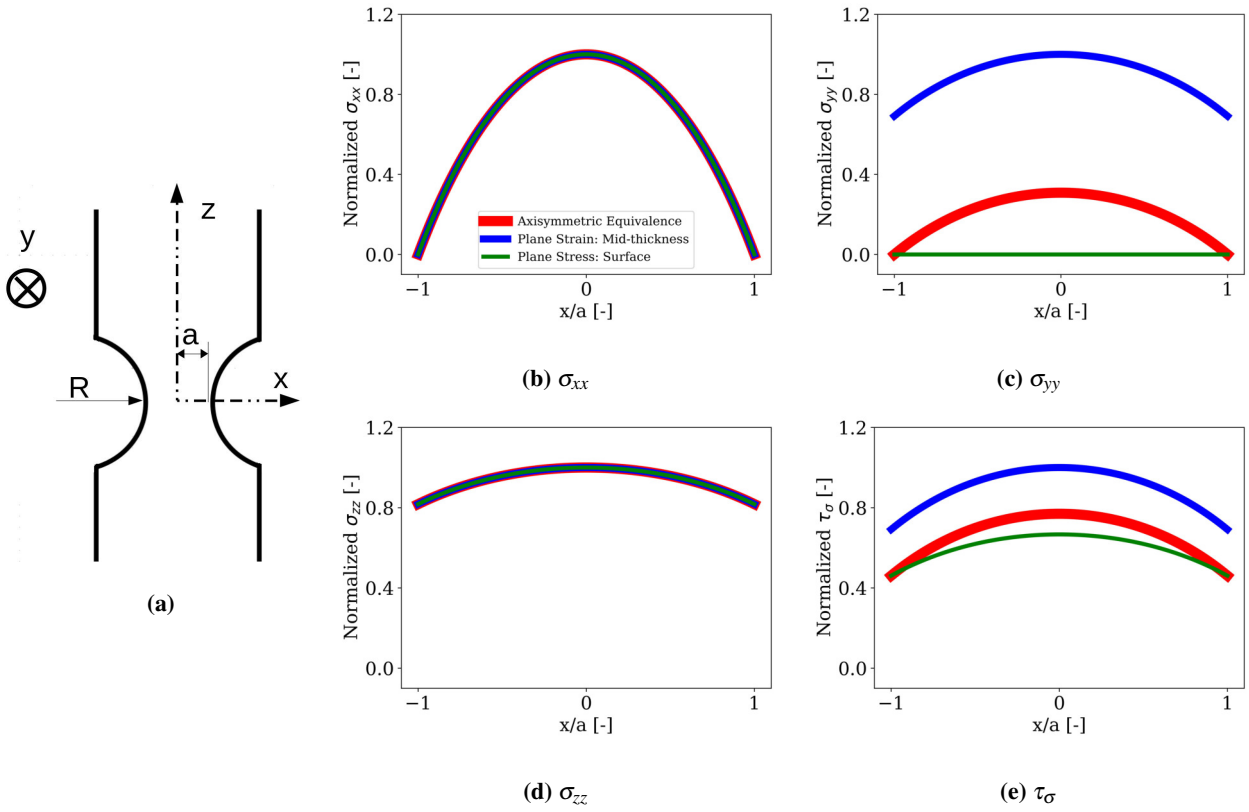

(a) **(b)** σ_{xx} **(c)** σ_{yy} **(d)** σ_{zz} **(e)** τ_σ

Figure 1: (a) Geometry of a notched specimen, and analytical stress state profiles along the notch root width: (b) σ_{xx}, (c) σ_{yy}, (d) σ_{zz}, (e) τ_σ

glass transition temeperature of PA11 were measured by DSC (Differential Scanning Calorimetry) and Tg was confirmed by DMA (Dynamic mechanical analysis).

Table 2: Physico-chemical properties of PE and PA11

	PE	PA11
Glass transition temperature T_g	-110 °C	53 °C
Melting temperature $T_{melting}$	110 °C	188 °C
Index of Crystallinity	Nc	20 %

Geometries In order to highlight the full 3D stress field mentioned above, flat notched samples were chosen in this work. The sample geometries of PA11 and PE are illustrated respectively in figure 2a and 2b. For PA11, smooth samples were initially obtained by injection process in a dumbbell-shape mold based on ISO527-1A standard, using a milling cutter a couple of symmetric notches with a curvature radius of 5 mm were then machined at the center zone. The total length

of the sample is 170 mm, its thickness is 4 mm, the minimum section at the notch root is 5 mm in width. The PE sample is 80 mm in total length, 10 mm in thickness, the notch was also machined by a milling cutter, except that the notch curvature radius R is bigger (5.5 mm), and the minimum section at the notch root is 5.7 mm * 10 mm.

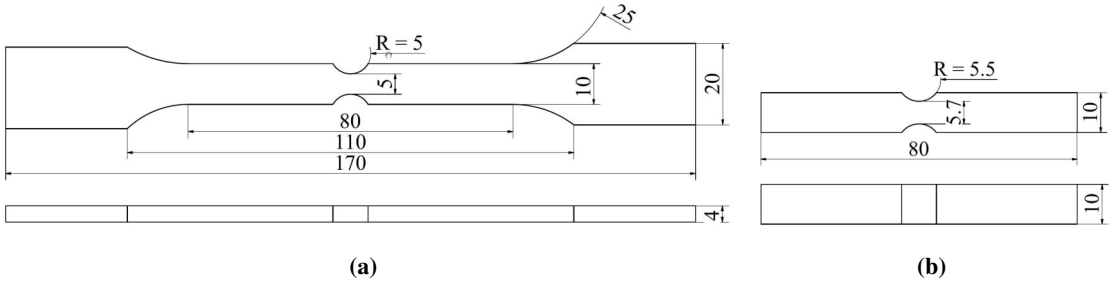

Figure 2: Sample geometry, unit: mm; (a) PA11: R = 5 mm, thickness = 4 mm, (b) PE: R = 5.5 mm, thickness = 10 mm

3.1.2 Testing protocol

Uniaxial tensile tests were carried out on an Instron machine with a load cell of 10 kN at room temperature. The PA11 specimens were tested under three cross-head speeds [1, 10, 100] mm/min, whereas the PE specimen was tested at a cross-head speed of 12 mm/min. During the test, an optical camera was used to record various displacements on the deformed specimen shape (geometrical variation). High accuracy infrared cameras (IR) were used to record the simultaneous surface temperature fields in video, both on the width and on the thickness, during the deformation. Two different infrared cameras were used for PA11, one in width, another in thickness. The IR camera for thickness is a FLUKE with an image acquisition frequency of 9 Hz, the other one for width is a FLIR SC7000 with an image acquisition frequency between 25 Hz and 168 Hz. For PE, only one FLIR camera was used to capture the temperature fields in both thickness and width, it was twisted concerning the normal to the width surface. The data was acquired at an acquisition frequency of 50 Hz. The experimental protocol characteristics are summarized in table 3. Each test was repeated twice for PA11.

Table 3: Experimental information

Materials	PA11	PE
Cameras	Optical camera + two IR cameras	Optical camera + one IR camera
Thermal image acquisition frequency	Thickness: 9 Hz, Width: 25 $\sim$ 168 Hz	50 Hz
Cross-head speed [mm/min]	1, 10, 100	12

3.2 Data processing

3.2.1 Geometrical variation

The notch opening length h_t is an important parameter for describing the local behavior of the notch and also for the verification of numerical model. It was measured by a home-developed tool *Ariane* that follows the virtual markers placed at each notch corner, the notch opening displacement Δh ($\Delta h = h_t - h_0$) was then computed. During the deformation, a smaller local curvature radius was developed at the notched root (depicted in figure 3), this phenomenon is known as re-necking [19, 26]. Meanwhile, the width $2a_t$ of the minimum section evolves during the deformation. As a consequence, the value of R_t and a_t at the notch root should be measured and updated for the determination of the analytical stress states from the Bridgman theory. The width $2a_t$ was measured by a home-developed tool *Dm_shadow* which allows detecting the minimum horizontal distance of the sample contour, the width reduction ratio, $\Delta a/a0$, was calculated. Using *Fiji* [29], R_t was determined analytically based on the coordinates of three points on the notch profile and confirmed by the superposition between the circle with a radius of R_t and the notch profile.

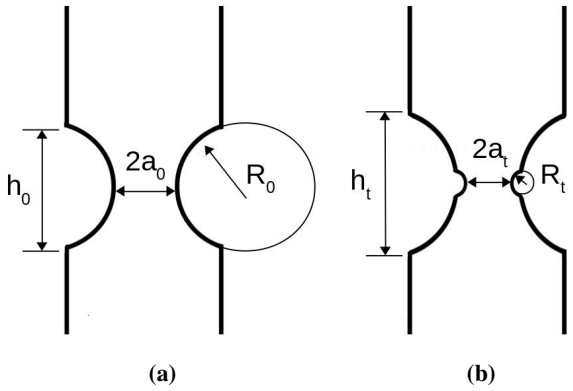

Figure 3: The measurements of notch opening displacement Δh (h_t - h_0), width $2a_t$, curvature radius R_t at: (a) undeformed state and, (b) deformed state. These displacements were synchronized with the load and the cross-head speed.

3.2.2 Whitening

During deformation, re-necking occurs when a necking with a smaller neck root radius appears inside the initial neck at the minimum width. Another phenomenon accompanied by re-necking is the whitening of sample surface, observed for both PA11 (figure 4) and PE. This phenomenon results from the alteration of materials optical characteristic due to internal void growth [30]. The whitening seems to intensify and extend from the mid-width towards the specimen shoulders during the deformation. In order to make it more visible, the original binary image was converted, using a python code, into colored image in function of their whitening intensity (from 0 to 250, 0

is for black, 250 for white) of each pixel. The intensity value of the whitened zone is between 160 and 250 where the contrast is significant compared to its vicinity. The length of whitening zone w in the tensile loading direction was measured and its evolution will be discussed in next section.

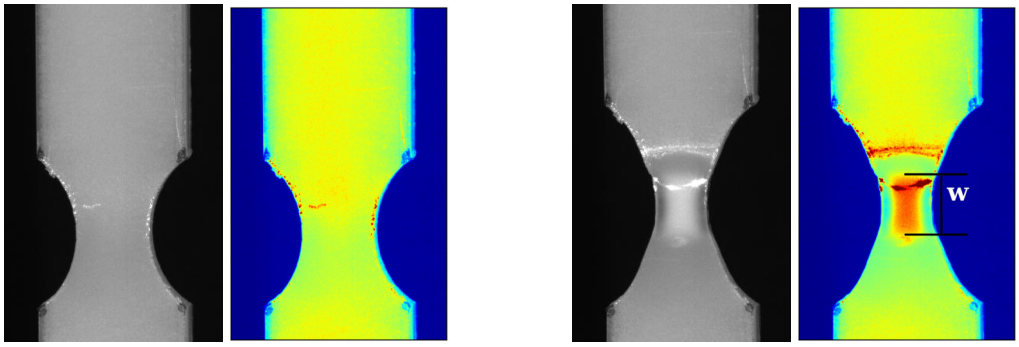

(a) **(b)**

Figure 4: Whitening of PA11 at: (a) undeformed state, (b) deformed state after peak load

4 Results

4.1 Mechanical response

4.1.1 Load versus applied displacement curves

Load evolution Figure 5a shows the load of PA11 as a function of the applied displacement at three cross-head speeds [1, 10, 100] mm/min. Two repeated tests for each cross-head speed are illustrated in the same figure. Figure 5b displays the evolution of load for PE at 12 mm/min, one single test was carried out. The load versus displacement curves of both materials exhibit the same trend and was highlighted in four major stages divided by dotted lines (see figure 5b): 1) the first stage corresponds to the linear load evolution at a small scale of deformation, 2) the second stage undergoes the nonlinear load evolution until the peak load, accompanied by the expansion of initial notch, 3) the third stage associates to the load-softening where occurs the re-necking and initiates the surface whitening around the notch, see figure 6, 4) the fourth stage consists of a load plateau during which the necked zone and the whitened one expand simultaneously in the tensile loading direction.

4.1.2 The evolution of whitening

Whitening distribution and spatial evolution The results of PA11 at 10 mm/min will be presented particularly due to the similar cross-head speed with PE (12 mm/min). Figure 6a shows the whitening

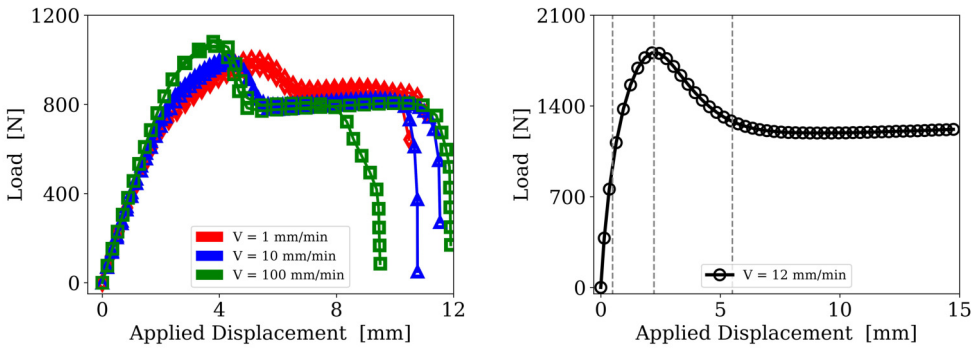

(a) PA11 **(b)** PE

Figure 5: The load evolution for: (a) PA11 at three cross-head speeds [1, 10, 100] mm/min, (b) PE at 12 mm/min

contour maps of PA11 at 10 mm/min. The image labelled as i, ii, iii, iv, v, vi were recorded respectively to the level of the applied displacement shown in the load versus applied displacement curve in the left figure: i is the initial state; ii is at the end of the linear load evolution; iii associates to the peak load; iv presents the middle load-softening; v relates to the end of load-softening; vi is during the load plateau. From the contour maps, the surface whitening evolves in the following order: 1) no apparent whitening was observed at the surface before the peak load (i, ii, iii), 2) whitening begins to appear around the mid-width of the notch root during the load-softening (iv), 3) the intensification of the whitening and radial extension essentially occur at the end of the load-softening (v), 4) the whitening zone extends along the loading direction during the load plateau, although the intensity weakens (vi).

A similar trend was observed for PE, see figure 6b. A whitening gradient was as well observed from the mid-width of the notch root towards its vicinity, this whitening gradient has been presented by [31].

Whitening length evolution The whitening length w versus applied displacement curves of PA11 for three cross-head speeds [1, 10, 100] mm/min are respectively displayed in figures 7a, 7b, 7c. The solid gray lines in each figure corresponds to the load evolution, given as a reference; besides, the dotted vertical lines divide the four mechanical stages defined above, the same usage for the upcoming results in this paper. The w has a similar evolution profile under different cross-head speeds. In line with our previous observations, no whitening was quantified prior to the peak load. Moreover, there is always a delay between the appearance of surface whitening and the peak load for the three cross-head speeds. It seems that the whitening length increases quasi-linearly with the applied displacement during the load-softening and the load plateau, however, with different rate. The slopes of w, increasing rate, at each stage were therefore calculated and summarized in

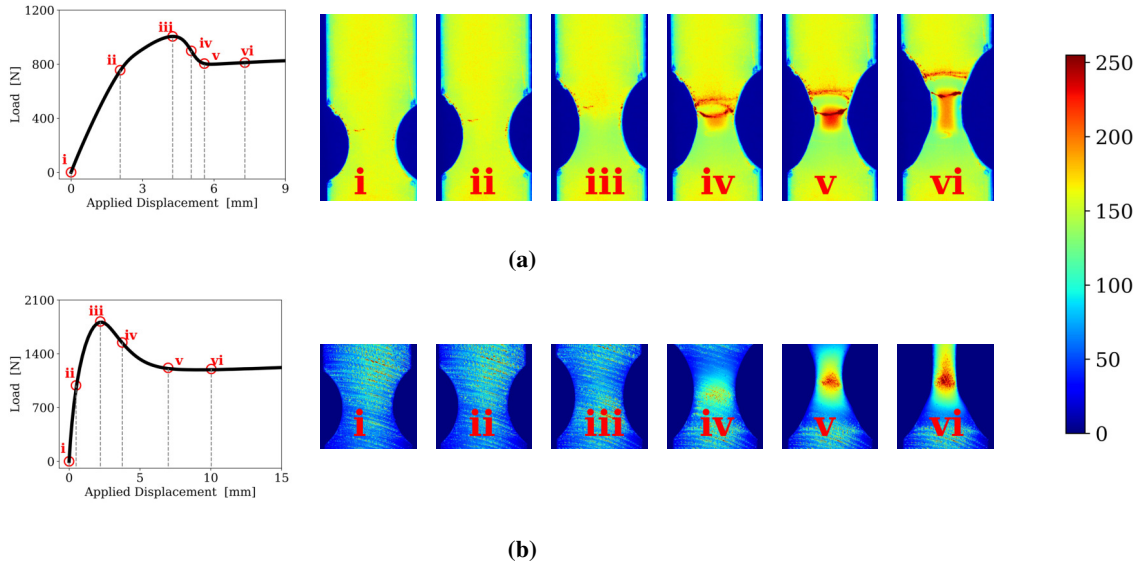

Figure 6: The whitening contour maps and the corresponding load-applied displacement evolution of: (a) PA11 at 10 mm/min, (b) PE at 12 mm/min

table 5 as well, their values at the end of each stage were summarized in table 4. Since similar w trends are presented regardless of the cross-head speed, the result at 10 mm/min will be taken as an example for the whitening evolution description: 1) no surface whitening was observed at the surface before the peak load, 2) the whitening initials after the peak load and reaches to 3.11 mm by the end of load-softening with an increasing rate of 2.68 mm/mm, 3) the surface whitens less quickly during the load plateau than during the load-softening with a smaller rate (1.19 mm/mm) .

Figure 7d displays the evolution of w for PE under 12 mm/min, similar results were obtained: 1) surface whitening appears slightly later after the peak load, 2) then w increases quasi-linearly during the load-softening with a rate of 1.54 mm/mm and finishes by 4.98 mm at the end of load-softening, 3) afterwards slows down the whitening rate (0.91 mm/mm) during the load plateau. Compared to PA11 at 10 mm/min, PE at 12 mm/min whitens less quickly during both the load-softening and the load plateau stage, however, a higher w value was measured for PE at the end of load-softening due to a longer period of load-softening.

A change of the slope w/ΔU occurs at the end of the load-softening, this change is clear for PA11 whatever the cross-head speed, a progressive softening tends to accelerate this change of the slope.

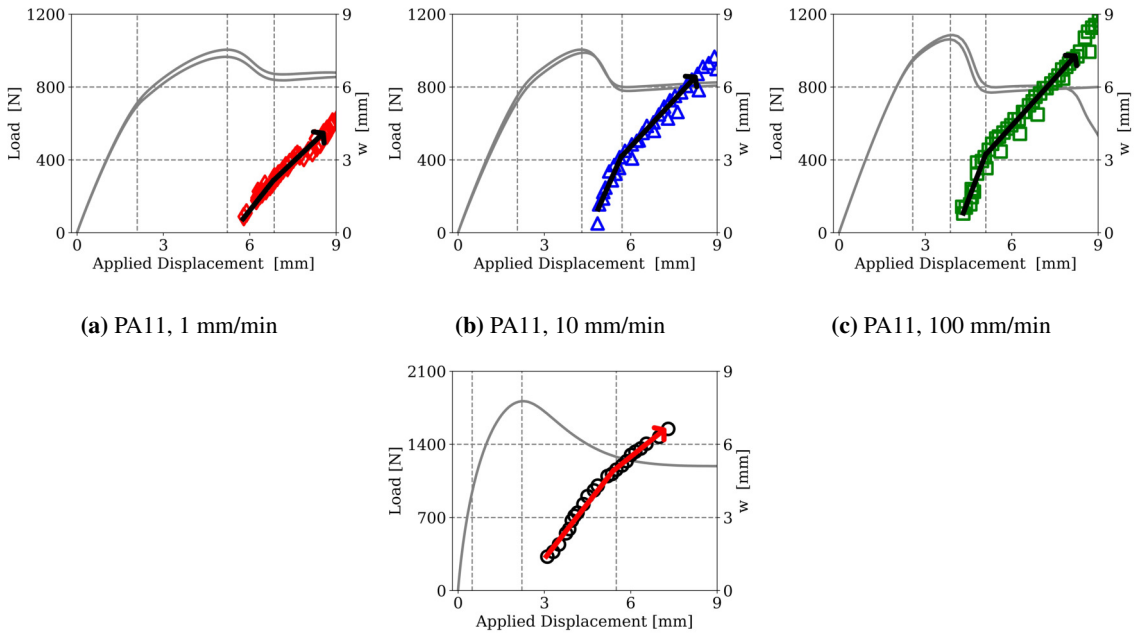

(a) PA11, 1 mm/min

(b) PA11, 10 mm/min

(c) PA11, 100 mm/min

(d) PE, 12 mm/min

Figure 7: The evolution of the whitening length w for: (a, b, c) PA11 at three cross-head speed [1,10,100] mm/min, (d) PE at 12 mm/min. The solid gray lines are the corresponding load evolution for each test.

Table 4: Values of w

	w [mm]			
	PA11			PE
V [mm/min]	1	10	100	12
Initial	-	-	-	-
End of linearity	-	-	-	-
Peak load	-	-	-	-
End of load-softening	2.21	3.11	3.16	4.98

Table 5: Slopes of w

	w/ΔU [-]			
	PA11			PE
V [mm/min]	1	10	100	12
Linear	-	-	-	-
Nonlinear	-	-	-	-
Load-softening	1.52	2.68	2.86	1.54
Load plateau	1.18	1.19	1.29	0.91

4.1.3 Measurements

Notch opening displacement evolution Figure 8a, 8b, 8c display respectively the notch opening displacement Δh of PA11 as a function of the applied displacement under three cross-head speeds [1, 10, 100] mm/min. With the load evolution as references, the Δh evolution seems to correlate well with the four mechanical stages defined previously. The Δh has the same evolution profile regardless of the cross-head speed: each stage presents a quasi-linear Δh increase subjected to the applied displacement. The slopes of each stage were determined and summarized in table 6, the Δh at the end of each stage were summarized in table 7 as well. Taking the example of the results at 10 mm/min, the Δh evolves in such order: 1) small increase rate of 0.21 mm/mm during

the linear load evolution, ending up to 0.42 mm at the end of the linear stage, 2) followed by a moderate increase with a rate of 0.46 mm/mm during the nonlinear stage and reaches 1.41 mm at the peak load, 3) then accelerates the notch opening during the load-softening with a rate of 1.14 mm/mm and arrives at 3 mm at the end of the load-softening, 4) finally slows down slightly with a rate of 0.97 mm/mm during the load plateau. The notch opening is the lowest during the linear stage, whereas it is the highest during the load-softening stage (Δh rate: linear ¡ nonlinear ¡ load plateau ¡ load-softening). During loading, except at the load-softening stage, the local notch opening displacement Δh is always inferior to the applied displacement, with a rate less than 1 mm/mm.

Figure 8d displays the Δh evolution of PE at 12 mm/min, a similar trend is presented: 1) the Δh begins with a moderate increasing rate of 0.40 mm/mm during the linear stage and ends up by 0.19 mm at the end, 2) then continues the increase with a slight higher rate of 0.46 mm/mm during the nonlinear stage and reaches 0.98 mm at the peak load, 3) afterwards followed by a significant notch opening rate of 1.05 mm/mm during the load-softening and attains 4.4 mm by the end of the load-softening, 4) finally finishes by the same increasing rate during the load plateau. In comparison with the results of PA11, the Δh evolution of PE differs from several facts: 1) the notch opens more quickly for PE at the beginning during the linear stage (0.2 mm/mm for PA11, 0.4 mm/mm for PE), 2) the notch opening doesn't slow down during the load-plateau, 3) the Δh level of PE is lower at the end of linear and non linear stage than at the end of the load-softening.

In line with a significant whitening rate during the load-softening, the notch opening displacement rate attains the highest as well during this period.

Width reduction evolution Figure 9a, 9b, 9c display the notch root width reduction ratio $\Delta a/a_0$ of PA11, in which a_0 is the initial half-width at notch root, Δa is the half-width reduction, as a function of the applied displacement for three cross-head speeds, [1, 10, 100] mm/min, respectively. A Z-trend evolution is highlighted, independently of the cross-head speed, which correlates fairly good with the load evolution. The slopes of each stage were calculated and summarized in table 6, as well as the $\Delta a/a_0$ values at the end of each stage in table 7. The width reduction evolution will be described using the example at 10 mm/min: 1) the width has almost no variation during the first linear stage with a reduction rate of -0.01 mm/mm, 2) then begins to slightly narrow during the nonlinear stage with a moderate decreasing rate of -0.04 mm/mm and end up by a reduction ratio of -0.1 mm/mm at the peak load, 3) a significant width reduction rate of -0.13 mm/mm undergoes during the load-softening, and the reduction ratios reaches to -0.29 mm/mm by the end of load-softening, 4) the width reduction finally slows down at a rate of -3.95 mm/mm and eventually

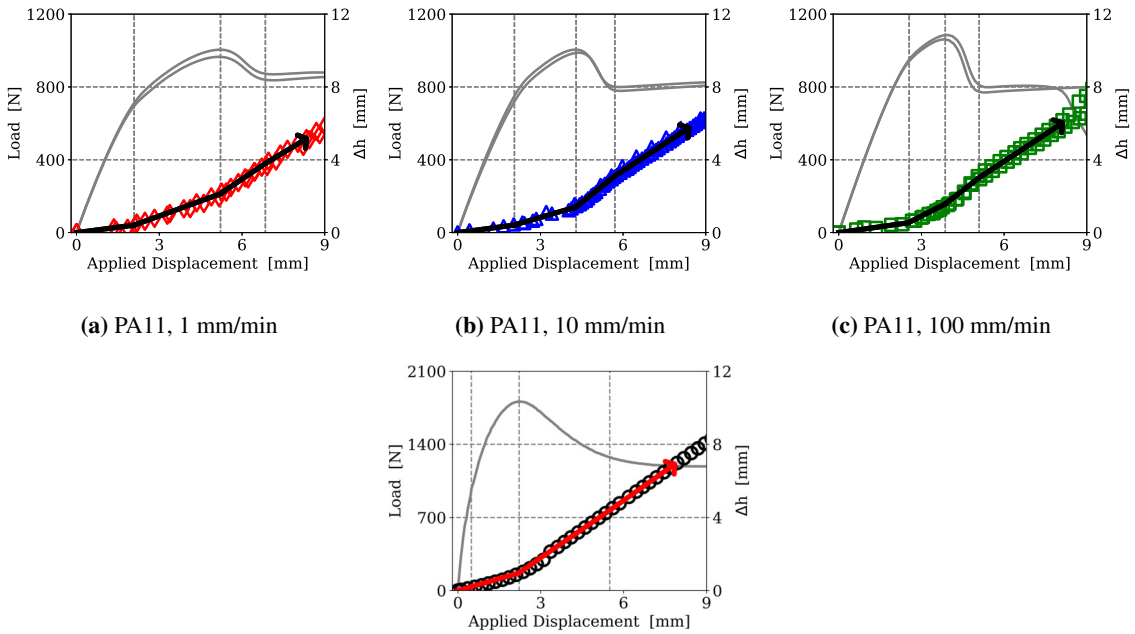

(a) PA11, 1 mm/min

(b) PA11, 10 mm/min

(c) PA11, 100 mm/min

(d) PE, 12 mm/min

Figure 8: The evolution of notch opening displacement Δh for: (a, b, c) PA11 at three different cross-head speeds, (d) PE at 12 mm/min.

stabilizes before rupture.

Figure 9d displays the width reduction of PE at 12 mm/min, the same evolution profile and similar results are obtained as that of PA11: 1) Nearly no width reduction was measured during the linear load evolution with a rate of -0.01 mm/mm, 2) similar reduction rate (-0.02 mm/mm) during the nonlinear stage, 3) significant shrinking rate (-0.09 mm/mm) of width during the load-softening, 4) the width reduction slows down slightly during the load-plateau with a rate of -0.06 mm/mm, the width reduced however 36.1 % at the end. Compared to PA11, the PE specimen narrows more quickly during the linear and load-plateau stage, but slower during the linear and load-softening stage. The final width reduction level is higher for PE than for PA11.

To be noted, the width reduction rate is highest during the load-softening, the situation is the same with the whitening length w and the notch opening displacement Δh.

Curvature radius evolution Figure 10a, 10b, 10c display the notch root curvature radius R as a function of the applied displacement of PA11 for three cross-head speeds, [1, 10, 100] mm/min, respectively. The red solid lines in figures were used to highlight the trend of the R evolution. A

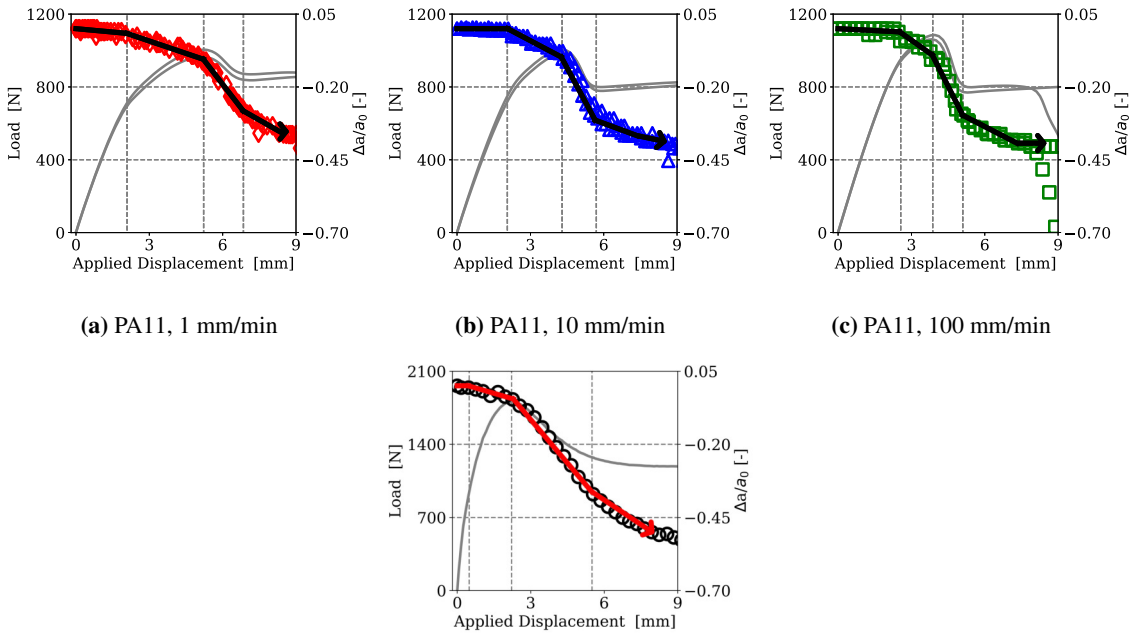

(a) PA11, 1 mm/min

(b) PA11, 10 mm/min

(c) PA11, 100 mm/min

(d) PE, 12 mm/min

Figure 9: The evolution of the width reduction ratio ($\Delta a/a_0$) for: (a, b, c) PA11 at three different cross-head speeds, (d) PE at 12 mm/min .

four stage evolution that correlates well with the mechanical response is obtained despite of the cross-head speed: R increases during the deformation except after peak load, where a dramatic drop is observed. Each stage consists of a quasi-linear variation of R, their slopes were calculated and summarized in table 6; furthermore, the R values at the end of each stage were as well summarized in table 7. The curvature radius R evolves in the following order taking the example of 10 mm/min: 1) Slight increase of R, during the first linear stage, from an initial value of 4.86 mm to 5.27 mm at a rate of 0.2 mm/mm, 2) During the nonlinear stage, a higher increasing rate of 0.63 mm/mm attaining 6.67 mm at the peak load, 3) Re-necking was observed during the load-softening, i.e. a smaller local curvature forms at the notch root, in which R decreases with a rate of 2.63 mm/mm attaining the minimum R value (1.68 mm) at the end of the load-softening stage, 4) the neck then extends, R increases towards infinite with a rate of 3.03 mm/mm during the load-plateau that finishes eventually as a smooth specimen.

The R evolution of PE is displayed in figure 10d, a similar trend, concerning PA11, is observed: 1) slight R increase during the linear stage with a rate of 0.62 mm/mm from 5.41 mm to 5.69 mm, 2) a higher increasing rate of 0.91 mm/mm during the non-linear stage, R ends up by 7.29 mm at peak load, 3) then a great decrease with a rate of 1.31 mm/mm during the load-softening and reaches the minimum R value at 3.16 mm by the end of the load-softening, 4) finally ends up by a steady R

increase with the rate of 2.28 mm/mm during the load-plateau where the notched specimen tends to be a smooth one. In comparison with the results of PA11 at 10 mm/min, the R of PE increases faster prior to the peak load, but variates less quickly during the load-softening as well as during the load-plateau. PE also has a higher level of initial curvature radius and minimum curvature radius by the end of load-softening.

For both materials, the re-necking phenomenon takes place at the load-softening, during which the notch root curvature radius R decreases abruptly and accompanied by a significant width reduction, the same phenomenon was obtained in the works of [19, 26].

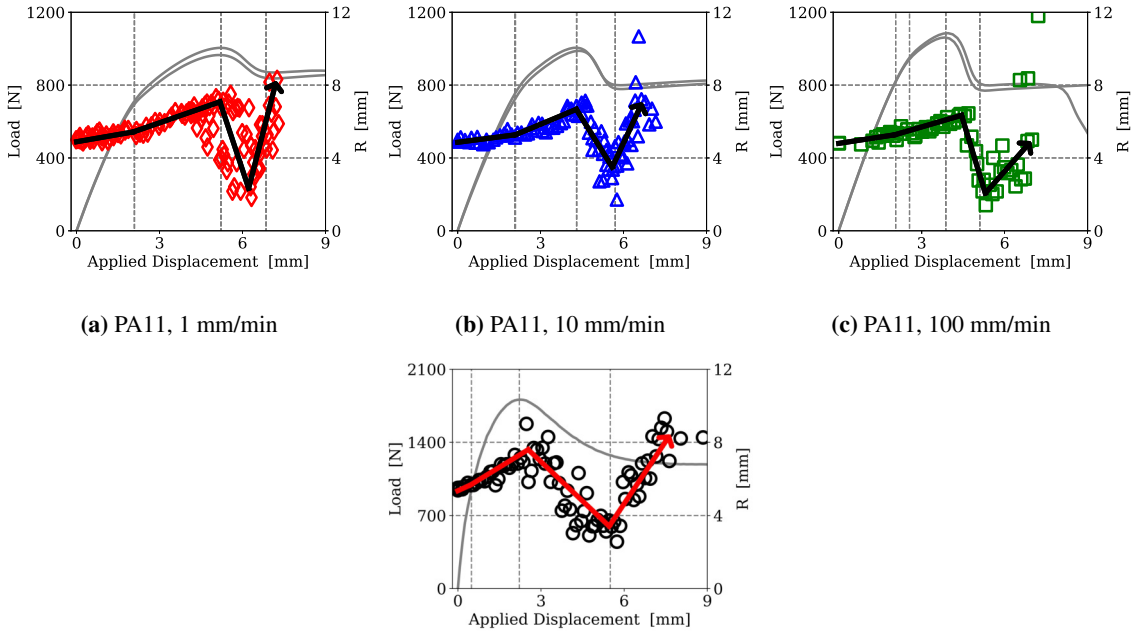

(a) PA11, 1 mm/min

(b) PA11, 10 mm/min

(c) PA11, 100 mm/min

(d) PE, 12 mm/min

Figure 10: The evolution of the notch root curvature radius R for: (a, b, c) PA11 at three different cross-head speeds, (d) PE at 12 mm/min.

4.1.4 Cross-head speed dependency

The tests on three different cross-head speeds of PA11 allow evaluation of the speed dependencies of mechanical responses, as well as the measured parameters presented previously.

Mechanical responses: load and displacement The cross-head speed dependency of mechanical responses will be discussed in terms of four parameters: the peak load (Fmax), the displacement

Umax at Fmax, the load at the end of the load-softening Fs and the displacement Us at Fs. Each term was normalized by the maximum value among all the tests completed. The terms at peak load (Fmax, Umax) and at the end of the load-softening (Fs, Us) are shown respectively in figure 11a and 11b. In line with previous studies [2, 13, 15, 16, 32, 33], the peak load increases with the cross-head speed; on the contrary, the Umax, Fs as well as the Us decrease with the cross-head speed. Therefore, a load-softening occurs earlier and is more severe at a higher cross-head speed.

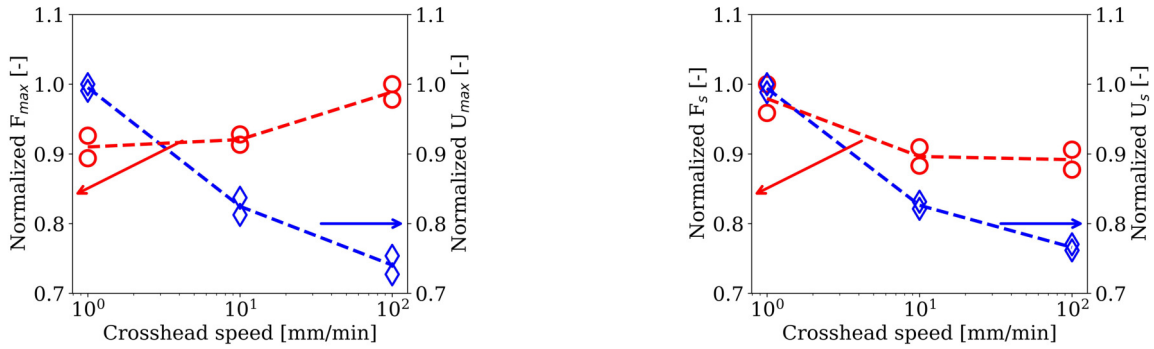

(a) Fmax **(b)** Umax

Figure 11: The cross-head speed dependency of mechanical responses of PA11: (a) the maximum load Fmax and the corresponding displacement Umax, (b) the load at the end of load-softening Fs and the corresponding displacement Us

Slopes of measured parameters Table 6 summarized the slopes at each stage of the three measured parameters (Δh, Δa/a0, R) subjected to applied displacement for all tests completed. The results show the notch opening displacement rate is nearly independent on the cross-head speed during the linear and the load plateau stage, but increases with the cross-head speed during the load-softening. In line with the notch opening rate, the width reduction rate increases with the cross-head speed during the non linear and the load-softening stage, however, less sensitive to the speed for the other two stages. For curvature radius R, it's relatively less influenced by the cross-head speed prior to the peak load, the re-necking rate increases with the speed during the load-softening, and decreases during the load plateau. In conclusion, the cross-head speed has generally less influences, prior to the peak load, on the measured parameters, but a significant impact especially during the load-softening stage.

Values of measured parameters The values at the end of each stage of the three measured parameters (Δh, Δa/a0, R) are summarized in table 7. The notch opening displacement Δh is highest at 100 mm/min at the end of the linear stage, and decreases slightly with the cross-head speed for the peak load and the end of the load-softening. The width reduction is less dependent on the speed at the end of the linear stage and the end of the load-softening, but reduces more at lower cross-head

Table 6: Slopes of Δh, Δa/a0, R

	Δh/ΔU [mm/mm]				Δa/a$_0$/ΔU [mm^{-1}]				R/ΔU [mm/mm]			
	PA11			PE	PA11			PE	PA11			PE
V [mm/min]	1	10	100	12	1	10	100	12	1	10	100	12
Linear	0.20	0.21	0.22	0.40	-0.01	-0.01	-0.01	-0.01	0.31	0.20	0.23	0.62
Nonlinear	0.54	0.46	0.67	0.46	-0.03	-0.04	-0.06	-0.02	0.51	0.63	0.44	0.91
Load-softening	0.99	1.14	1.29	1.05	-0.11	-0.13	-0.17	-0.09	-2.51	-2.63	-4.98	-1.31
Load plateau	0.98	0.97	0.97	1.05	-0.04	-0.04	-0.04	-0.06	7.16	3.03	1.73	2.28

speed at the peak load. As for curvature radius R, the higher the cross-head speed, the lower the R at the peak load and the end of the load-softening. To conclude, the measured values at the end of each stage are less sensitive to cross-head speed prior to peak load, slightly influenced at peak load or at the end of the load-plateau.

An increase of all rates was occured during the load-softening, during which the void growth attains the maximum value through tomography results [27].

Table 7: Values of Δh, Δa/a0, R

	Δh [mm]				Δa/a0 [-]				R [mm]			
	PA11			PE	PA11			PE	PA11			PE
V [mm/min]	1	10	100	12	1	10	100	12	1	10	100	12
Initial	0	0	0	0	0	0	0	0	4.89	4.86	4.8	5.41
End of linearity	0.42	0.42	0.55	0.19	-0.01	-0.01	-0.01	-0.01	5.43	5.27	5.27	5.69
Peak load	2.09	1.41	1.39	0.98	-0.10	-0.10	-0.09	-0.05	7.08	6.67	6.34	7.29
End of load-softening	3.67	3	2.98	4.4	-0.27	-0.29	-0.29	-0.36	1.81	1.68	1.46	3.16

4.2 Thermography Results

Emissivity qualifies the materials ability of emitting radiation, it is therefore an important parameter for an accurate temperature measurement using IR camera [34]. The emissivity reduces when PA11/PE whitens, it drops generally from 0.97 to around 0.9 during the deformation. With such emissivity variation, the maximum error of measured temperature is less than 4%. Such difference is assumed to be negligible, so, a uniform emissivity of 0.95 was applied to all the tests.

4.2.1 Temperature variation measurement at the surface

Figure 12 shows the heat build-up temperature evolution of PA11 and PE during deformation at a cross-head speed of 10 mm/min and 12 mm/min, respectively. The measured temperature through

the width and the thickness of PA11 at cross-head speed 10 mm/min are shown respectively in figure 12a and 12b. The solid gray plots in the left figures are the corresponding load-applied displacement curves. The temperature contour maps correspond to the applied displacement: i is the initial temperature, ii relates to the temperature at the end of the linear stage, iii corresponds to the temperature at peak load, iv associates with the temperature at the end of the load-softening, v represents the temperature at the end of the load plateau, vi is the temperature at rupture.

Temperature distribution and spatial evolution The maximum temperature is identified by a black cross in each temperature contour maps. The maximum temperature rise ΔT_{max} (T_{max} - $T_{ambient}$) and the loading time t are indicated as well. The temperature variation is similar through width and through thickness except at rupture. For the reason of simplicity, only the heat build-up in thickness is to be discussed.

According to the thermography results: i) the PA11 specimen under 10 mm/min has an initial ambient temperature of 20.6 °C, ii) a slight temperature decrease of -0.3 °C, linked with the thermoelastic response, was measured during the linear stage, iii) a negligible heat build-up temperature of 1.9 °C initials at the notch surface at peak load, iv) a significant temperature rise (10.6 °C) was measured at the end of the load-softening in a short time (8 seconds), v) a slight heat build-up of 3.3 °C was measured at the end of the load-plateau, vi) a huge amount of heat was generated during crack propagation.

The mid-width/mid-thickness at the minimum section were marked by gray dotted lines. The maximum temperature (black cross) is not located at the same position, i.e. up to the end of the load softening it is located near the mid-width and mid-thickness at the minimum section (iv) then it is located at the notch shoulder (v) or the rupture facies (vi). The temperature field is heterogeneous through both width and thickness, the heating zone intensifies and extends progressively along the loading direction during the deformation.

The thermography results of PE through the thickness are displayed in figure 12c. A similar heat build-up evolution was measured: i) the specimen was tested at an ambient temperature of 28.3 °C, ii) a slight temperature decrease of -0.4 °C was measured at the end of the linear stage, iii) the similar temperature decrease was maintained during the nonlinear stage, iv) an important temperature rise (6 °C) occurs at the end of the load-softening, v) slight temperature increase during the load-softening, vi) the specimen ends up with a significant temperature rise (18.7 °C) at rupture. Compared to PA11, both materials have an heterogeneous temperature field. A significant heat build-up temperature of PE was observed solely after the peak load (iv). Their maximum temper-

ature locates both more or less around the mid-thickness then dislocates to the notch shoulder (v) or rupture facies (vi).

Time evolution The red curves in the figure 12a and 12b are the evolution of the maximum temperature rise ΔT_{max} for PA11 at 10 mm/min in width and in thickness respectively. It seems that the heat build-up evolution correlates well with the four-stage load evolution. The slopes of ΔT_{max} at each stage were calculated and summarized in table 8. The final temperature Tend and temperature variation ΔT of each stage were summarized in table 9. Taking the heat build-up through the thickness of PA11 at 10 mm/min as an example, the evolution is as follows: 1) slight decrease (-0.3°C) during the linear stage with a rate of -0.15, 2) negligible temperature rise (1.9 °C) with an increasing rate of 0.77 during the nonlinear stage, 3) significant temperature rise (10.6 °C) with a considerable increasing rate of 10 during the load-softening, 4) finishes by a slight temperature rise (3.3 °C) during the load plateau with a rate of 0.6. During the deformation, the temperature rise occurs principally at the load-softening stage.

In line with the previous results of geometrical parameters, the first significant temperature increases occurs during the load-softening.

4.2.2 Heat build-up profile at the notch root

From the temperature contours presented above, a temperature gradient, from the mid-width and mid-thickness towards the borders, are observed. In order to verify the temperature gradient, the temperature rise ΔT during deformation was plotted, see figure 13. Figure 13a and 13b display the ΔT profiles of PA11 through thickness and through width at minimum section under 10 mm/min, figure 13c displays the ΔT profile of PE through thickness. Each ΔT profile in the figure relates to the applied displacement illustrated in the top-right load-displacement plot. The heat build-up temperature profile of both the mid-width and the mid-thickness, before the end of the load-softening, show a trapezoid trend at the center and decreases towards the notch root; however, the maximum temperature moves towards the border prior to the rupture. The similar phenomenon was observed for thickness: a ΔT plateau around the mid-thickness and decreases towards the surface. As for PE, ΔT was quasi-constant though thickness until the load-softening, an inverted parabola profile was then prevailed while the peak temperature rise locates at the mid-thickness and decreases towards the surface. The ΔT profiles become irregular during the load plateau where the maximum temperature rise dislocates towards the notch shoulder or surface.

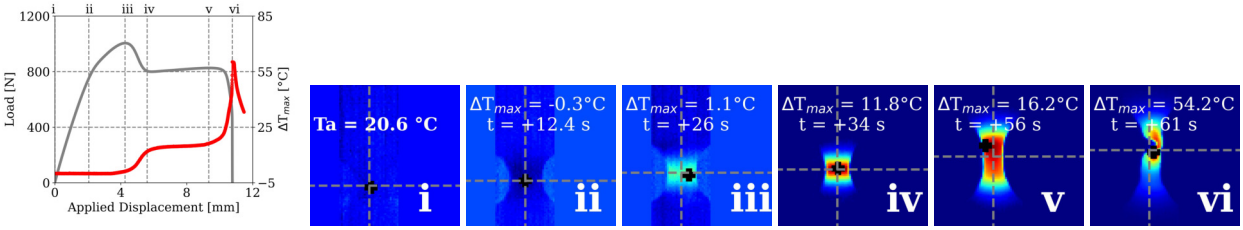

(a) PA11, 10 mm/min, Width

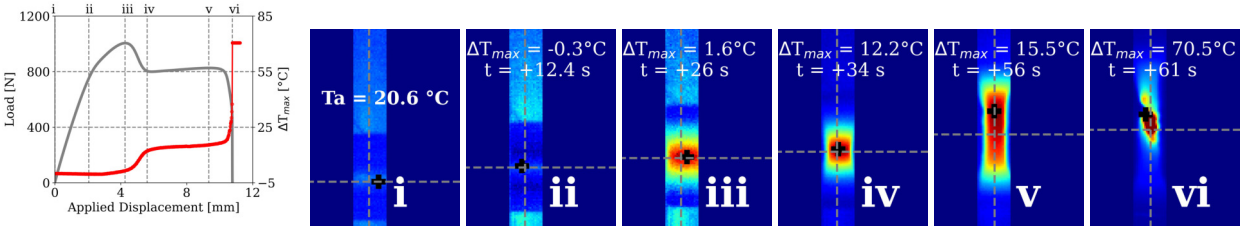

(b) PA11, 10 mm/min, Thickness

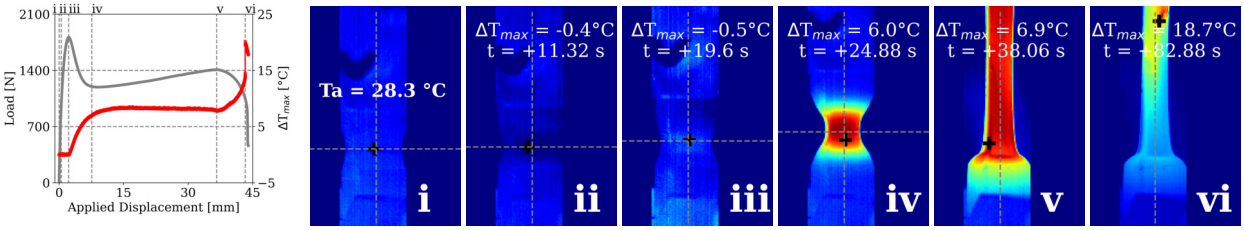

(c) PE, 12 mm/min, Thickness

Figure 12: The evolution of load and ΔT_{max} for: (a) PA11 in width at 10 mm/min, (c) in thickness at 10 mm/min, (e) PE in thickness at 12 mm/min. Surface temperature contour maps for: (b) PA11 in width at 10 mm/min, (d) in thickness at 10 mm/min, (f) PE in thickness at 12 mm/min.

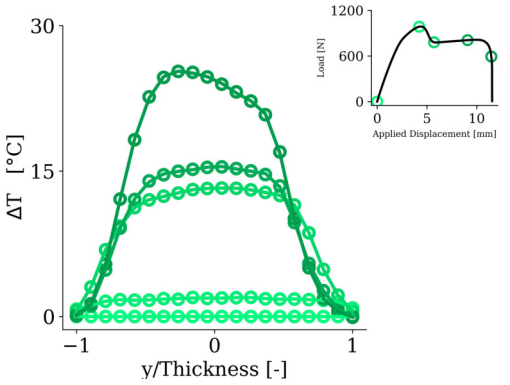

(a) PA11, thickness, 10 mm/min

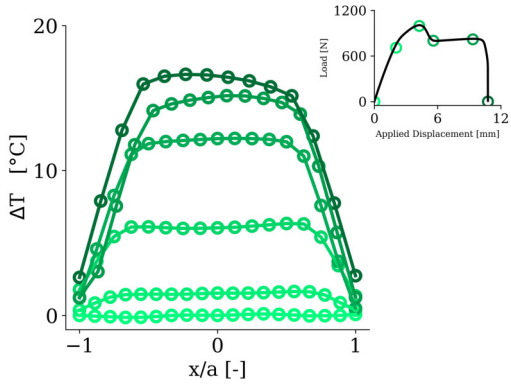

(b) PA11, width, 10 mm/min

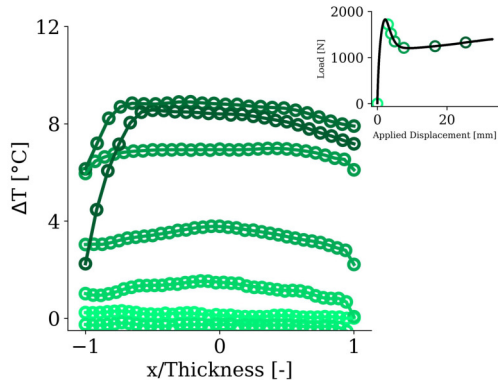

(c) PE, thickness, 12 mm/min

Figure 13: Temperature profile at the notch root for: (a) PA11 in width at 10 mm/min, (b) PA11 in thickness at 10 mm/min, (c) PE in width at 12 mm/min.

4.2.3 Cross-head speed influences on heat build-up

Cross-head speed influences on spatial evolution Figure 14 displays the load and ΔT_{max} evolution as well as the surface temperature contour maps of PA11. The figure 14a, 14c 14e display the results through width at three cross-head speeds respectively. The figure 14b, 14d, 14f display the results in thickness for three cross-head speeds respectively. The presentation and details contained in each temperature contour maps are the same as described previously for 10 mm/min. The temperature fields are heterogeneous at the surface both in width and in thickness, the temperature intensifies during the deformation and extends along the loading direction and the surface/notch root. From the measured temperature, the ambient temperature of specimens at three different cross-head speed is slightly different, but the heating phenomenon is similar: 1) slight decrease at the end of linear stage except specimen width at 1 or 100 mm/min; 2) a small temperature rise at the peak load; 3) a significant temperature rise by the end of the load-softening; 4) a temperature rise depends strongly on the cross-head speed during the loading plateau; 5) a significant heat generation at rupture. The maximum temperature is located around the mid-width/mid-thickness, up

to the load plateau, then it is displaced towards the notch shoulder or the crack path.

Cross-head speed on time evolution Table 8 summarized the slopes of ΔT_{max} at each stage for different tests. Table 9 summarized the final temperature Tend and temperature variation ΔT of each stage for all the test completed. From the tables, the cross-speed has no significant influence on the linear stage, for the other stages, however, the higher the cross-head speed: 1) the quicker the temperature rises, 2) the higher the temperature variation ΔT and the higher the final temperature Tend at each stage.

Table 8: $\Delta T_{max}/\Delta U$ [°C/mm]

	PA11			PE
V [mm/min]	1	10	100	12
Linear	-0.18	-0.15	0.01	-0.44
Nonlinear	0.21	0.77	3.55	0
Load-softening	1.95	10.00	21.18	1.31
Load plateau	-0.18	0.60	8.73	-0.01

Table 9: Temperature at each stage though thickness

V [mm/min]	PA11, thickness						PE, thickness	
	1		10		100		12	
	Tend [°C]	ΔT [°C]	Tend [°C]	ΔT [°C]	Tend [°C]	ΔT [°C]	Tend [°C]	ΔT [°C]
Linear	18.5	-0.4	20.3	-0.3	21.1	-0.2	27.9	-0.4
Nonlinear	19	0.5	22.2	1.9	24	2.9	27.8	-0.1
Load-softening	21.2	2.2	32.8	10.6	51.3	27.3	34.3	6.5
Load plateau	21	-0.2	36.1	3.3	69.3	18	35.2	0.9
Rupture	90.8	69.8	91.1	55	92.1	22.8	47	11.8

Cross-head speed influence on ΔT profile Figure 15 display the ΔT profile of PA11 for three cross-head speeds tested. The three rows display respectively the ΔT profile for each speed. The first column is the ΔT profile in width, the second column is in thickness. Each profile curve corresponds to the applied displacement illustrated in their top-right load-applied displacement plot. Regardless of the cross-head speed, the ΔT profile in width or thickness is either an inverted parabola or trapeze profile, up to the end of the load plateau, in which the maximum temperature locates around the mid-width/mid-thickness, and a temperature gradient presents from the mid-width/mid-thickness to its extremity.

5 Discussion

5.1 Stress state evolution

Stress triaxiality ratio distribution Using the analytical τ_σ equation, at plane strain hypothesis, presented in Section 2, the spatial distributions of τ_σ of PA11 along the sample width at two important loading states (peak load Fmax and the end of load-softening Fs) were determined and displayed respectively in figure 16a and 16b for different cross-head speeds. The corresponding load *F*, half-width *a* and curvature radius *R* at the two loading states are summarized in table 10. Whatever the cross-head speed, the profile of τ_σ along width is an inverted parabola where the max τ_σ locates at the mid-width and decreases to 0.5 at the notch root (x = a). The τ_σ at Fmax is not sensitive to the cross-head speed, however, the maximum τ_σ (at mid-width, x = 0) at the end of the load-softening Fs increases with the cross-head speed. The maximum τ_σ is higher at the end of the load-softening than at peak load, the gap is especially high at higher cross-head speed. The same τ_σ profiles are obtained for PE at 12 mm/min, see fig 16c and 16d , a similar τ_σ level was found at mid-width with the result of PA11 at 10 mm/min.

Table 10: The values of F, a and R at Fmax and Fs

	PA11						PE
V [mm/min]	1		10		100		12
Fmax [N]	1003	965	1005	987	1061	1083	1816
Fs [N]	870	834	797	771	769	798	1274
a_{max} [mm]	2.28	2.28	2.33	2.28	2.12	2.30	2.76
a_s [mm]	1.85	1.85	1.80	1.80	1.70	1.70	1.80
R_{max} [mm]	7.00	7.17	6.86	6.31	6.02	6.24	7.29
R_s [mm]	4.50	4.50	2.86	2.86	1.39	1.39	3.00

Stress triaxiality ratio evolution According to the spatial distribution of τ_σ presented above, the stress triaxiality ratio is highest at sample center (x = 0). Its time evolution was, then, calculated with the updated *F, a, R* that measured previously. Figure 17a, 17b, 17c display the evolution of stress triaxiality ratio τ_σ at the sample center for PA11 at three cross-head speeds [1, 10, 100] mm/min respectively. The τ_σ exhibits the same trends regardless of the cross-head speed: 1) it begins by a slight decrease, up to the peak load, 2) then a sudden increase during the load-softening and, 3) finishes by a dramatic drop during the load-plateau. The initial and final value of τ_σ at each stage (τ_{init} and τ_{end}), as well as their slopes are summarized in table 11. Taking the example of results at 10 mm/min, the stress triaxiality ratio at the sample center evolves in the following way: 1) τ_σ remains nearly the same value during the linear stage (from 0.73 to 0.71)

with a negligible decreasing rate of -0.01 mm^{-1}, 2) then slightly decreases from 0.71 to 0.67 at the rate of -0.02 mm^{-1} during the nonlinear stage, 3) afterwards increases with a rate of 0.09 mm^{-1} during the load-softening, 4) finally reduces significantly during the load plateau with a high rate of -0.19 mm^{-1}. Figure 17d displays the similar results for PE at 12 mm/min. A similar trend was obtained, τ_σ has: 1) almost the same decreasing rate during the linear and non-linear stage, 2) a slight increase with a moderate increasing rate of 0.07 mm^{-1} during the load-softening, 3) then finishes by a steady drop with a rate of -0.08 mm^{-1}. Compared with the τ_σ change of PA11 at 10 mm/min, PE has the similar variation rate except the τ_σ is lower at the end of the load-softening.

Cross-head speed dependencies on τ_σ The initial and final value of τ_σ at each stage (τ_{init} and τ_{end}), as well as their slopes at three cross-head speeds, [1, 10, 100] mm/min, of PA11 are summarized in table 11. The cross-head speed has barely no influence on the linear and nonlinear stage and the cross-head speed below 10 mm/min; however, a significant influence on the load-softening and load-plateau is shown between 10 and 100 mm/min: the higher the cross-head speed, the higher the τ_σ and its variation rate.

In line with the previous results of geometrical measurements and the heat build-up, a remarkable transition was observed for all of them during the load-softening period, this may link to the higher level of stress triaxiality.

Table 11: The values and slopes of τ_σ at each stage

V [mm/min]	PA11, thickness									PE, thickness		
	1			10			100			12		
	τ_{init} [-]	τ_{end} [-]	$\Delta\tau/\Delta U$ [/mm]	τ_{init} [-]	τ_{end} [-]	$\Delta\tau/\Delta U$ [/mm]	τ_{init} [-]	τ_{end} [-]	$\Delta\tau/\Delta U$ [/mm]	τ_{init} [-]	τ_{end} [-]	$\Delta\tau/\Delta U$ [/mm]
Linear	0.73	0.71	-0.01	0.73	0.71	-0.01	0.72	0.70	-0.01	0.74	0.73	-0.02
Non-linear	0.71	0.65	-0.02	0.71	0.67	-0.02	0.70	0.69	-0.02	0.73	0.68	-0.03
Load-softening	0.65	0.77	0.08	0.67	0.92	0.09	0.67	1.1	0.29	0.68	0.81	0.07
Load plateau	0.77	-	-0.18	0.78	-	-0.19	1.1	-	-0.32	0.81	-	-0.08

The maximum principal stress distribution The maximum principal stress σ_{zz} distribution along the minimum width of PA11 at Fmax and Fs, based on the plane strain hypothesis of Bridgman theory, are calculated and displayed respectively in figure 18a and 18b. The inverted parabola profile shows a maximum σ_{zz} at mid-width and decreases towards the notch root. The σ_{zz} difference seems to be small below 10 mm/min and close between peak load and the end of the load-softening, except a higher level of σ_{zz} was obtained at 100 mm/min. Figure 18c and 18d display the results

for PE at 12 mm/min, a higher level of σ_{zz} was obtained for PE (the maximum σ_{zz} of PE is more than 80 MPa, PA11 less than 80 MPa). The distributions of other principal stresses are displayed in Appendix.

Time evolution of maximum principal stress The time evolution of three principal stresses at mid-width of minimum cross-section were studied. The evolution of maximum principal stress σ_{zz} of PA11, for three cross-head speeds [1, 10, 100] mm/min, are displayed respectively in figure 19a, 19b, 19c. The evolution of two other principal stresses are displayed in Appendix. The σ_{zz} seems keeping increasing non-linearly during the deformation except at the load-softening period: a σ_{zz} drop presents during the load-softening, this drop becomes more significant with the increase of the cross-head. Figure 19d displays the σ_{zz} evolution for PE at 12 mm/min, the similar trends is obtained: a nonlinear increasing was observed from the beginning of the deformation, while a slight decrease is presented during the load-softening as observed for PA11. At a given applied displacement, the PE has generally a lower σ_{zz} level than PA11.

5.2 Comparison of theoretical stress state and ΔT

The profiles of theoretical stress triaxiality ratio and three maximum principal stresses along the sample width depend on a common term $log[1+\frac{a}{2R}(1-\frac{x^2}{a^2})]$, which exhibits an inverted parabola for all the stress state term, as shown in figure 20a. The ΔT profile that measured experimentally was normalized and superimposed with the stress state profile in figure 20a. Through figure 20a, a good correlation between stress state and heat build-up is presented: an inverted parabola profile was obtained for both parameters, a maximum stress state and heat build-up are located at the mid-width, and decreases towards the notch root. Concerning the thickness, the normalized experimental ΔT profile is displayed in figure 20b. For a flat sample, no theoretical stress state has been ever developed through its thickness, this type of sample is always considered as a 2D problem where the stress is independent of the thickness. Nevertheless, the surface of a flat specimen is, indeed, on plane stress whereas the mid-thickness on plane strain; therefore, a higher stress state on the mid-thickness, than the one on the surface, is expected. The results then correlates well with the trapeze/inverted parabola ΔT profile through thickness. The heterogeneous ΔT profile through thickness reveals, thus, a possible stress gradient. In this situation, the traditional 2D modeling of flat specimen is not accurate enough, the stress condition is not simply plane strain neither plane stress, it's strongly recommended to carry out a 3D numerical modeling if possible to take into account the stress heterogeneity.

It should be noted that the evolution of void volume fraction [26] is in line with ΔT, σ_{zz}, τ_σ as presented here.

6 Conclusions

This study deals primarily with the stress heterogeneity effects on the heat build-up of two semi-crystalline polymers (PA11 and PE), analytical and experimental methods were applied to flat notched specimen where their heterogeneous theoretical stress states (σ_{xx}, σ_{yy}, σ_{zz}, τ_σ) were computed and simultaneous surface temperature fields were measured.

The paper first summarized, based on Bridgman theory, the theoretical stress state distributions of notched flat sample at minimum cross section. In order to take into account the stress difference in thickness, the authors completed the stress state fields with plane stress hypothesis, in addition to plane strain and axisymmetric equivalence hypotheses. According to the theoretical analyses, the stress states decrease from mid-width toward notch root, and the stress level is higher in mid-thickness than at the surface.

The uniaxial tensile tests at different cross-head speeds were carried out on PA11 and PE. Their geometrical parameters (Notch opening displacement, width reduction, curvature radius) and surface whitening were post-processed, the analytical stress states were computed. The surface temperature fields in width and thickness were analyzed.

Regardless of the material, the experimental results show a good correlation between mechanical responses, geometrical evolution, surface whitening and the stress states as well as the heat build-up. A four-stage evolution was defined for these parameters: 1) during the first linear load stage, no apparent variation was observed for these parameters, 2) during the nonlinear load evolution up to the peak load, the evolution of these parameters are fairly smooth, 3) during the load-softening stage, a significant transition was measured and observed for the surface whitening, geometrical parameters, stress states, as well as the temperature rise, 4) during the load-plateau, these parameters change become again smooth.

From thermal fields, heterogeneous temperature fields were observed at sample surface. The heat build-up profiles at notch root demonstrate a temperature gradient in both thickness and width. This thermal profile correlates well with the stress state profile: a higher heat build-up was measured at higher stress level.

Similar conclusions were obtained for two semi-crystalline polymers with total different glass transition temperatures, which implies the heat build-up phenomenon and thermomechanical coupling is independent of materials for semi-crystalline polymers.

One remarkable result of this study is that the heat build-up is heterogeneous in thickness, which implies a heterogeneous stress state through thickness and the necessaries of 3D numerical modeling for such geometry to obtain more accurate results, instead of assuming plane strain or plane stress. The future work will, thus, work on 3D numerical modeling in taking into account the heat build-up in order to predict the interior heat build-up and to confirm the heterogeneous stress state in thickness. The investigation of stress heterogeneity effects on heat build-up will also be carried out on pre-cracked specimens whose stress state is completely different with that of the flat notched specimen.

7 Acknowledgments

The authors wish to extend their gratitude to Nathan Odou for the raw experimental database on PolyEthylene and Henri-Alexandre CAYZAC (Arkema) for his fruitful discussion to this research work. The authors acknowledge also their gratitude to Arkema for its financial supports.

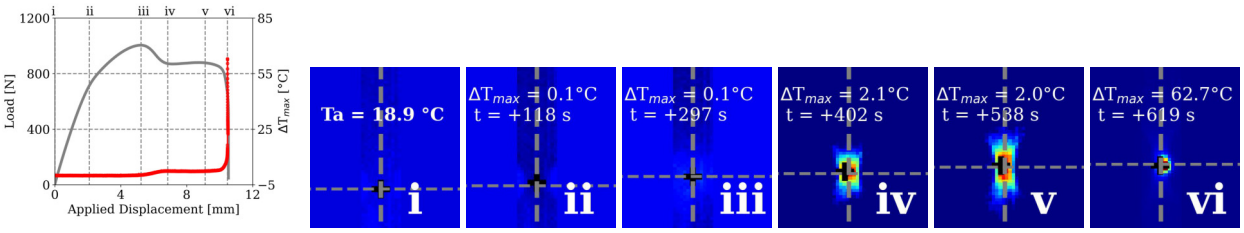

(a) PA11, 1 mm/min, Width

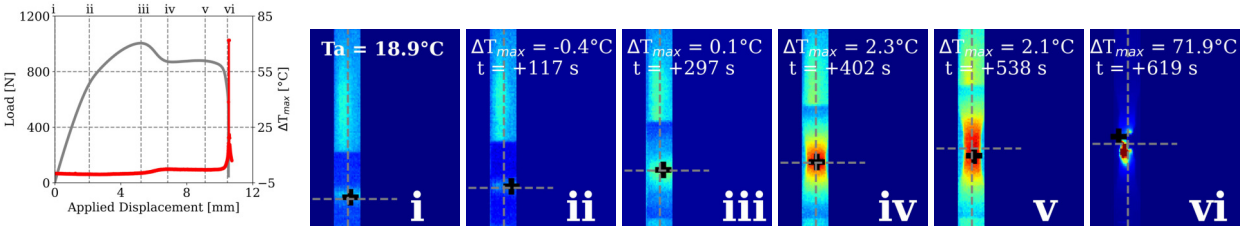

(b) PA11, 1 mm/min, Thickness

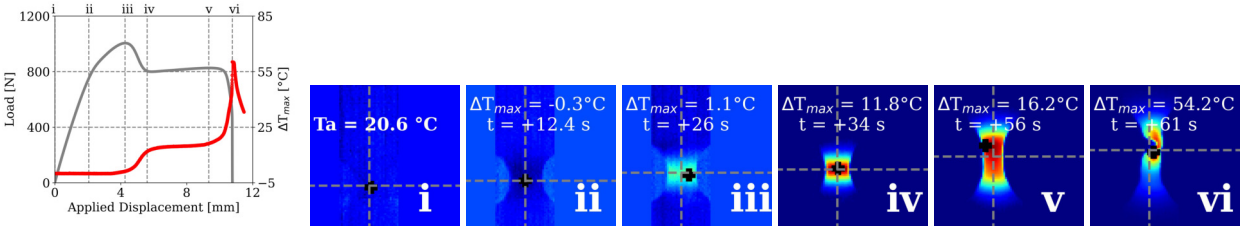

(c) PA11, 10 mm/min, Width

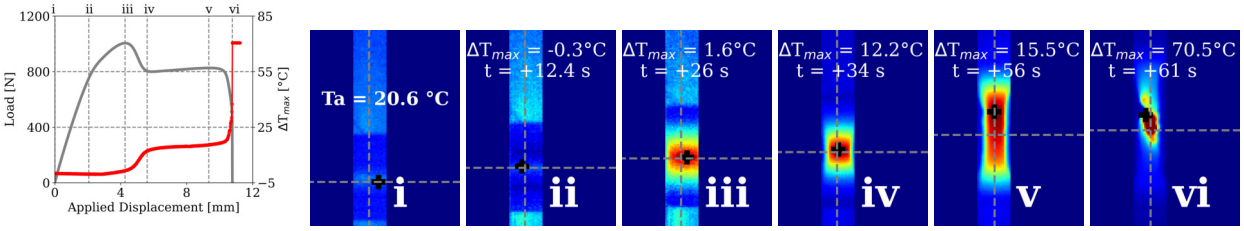

(d) PA11, 10 mm/min, Thickness

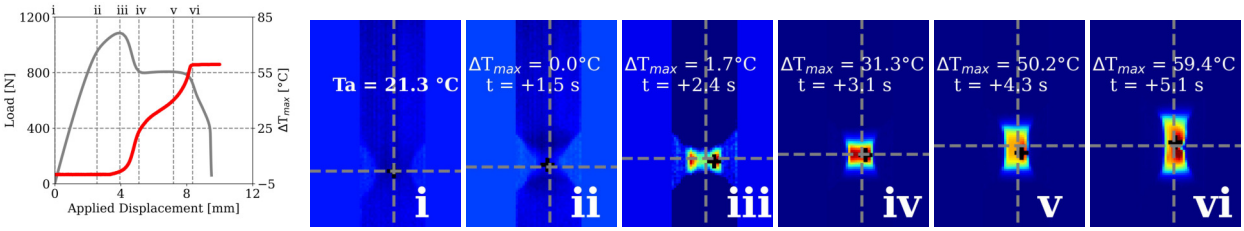

(e) PA11, 100 mm/min, Width

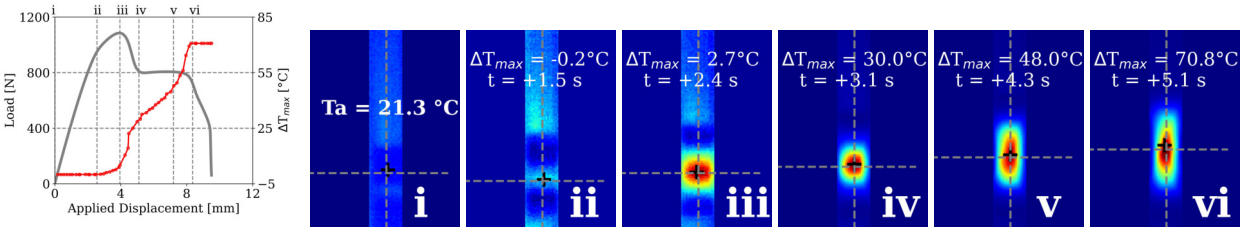

(f) PA11, 100 mm/min, Thick

Figure 14: The evolution of load and ΔT_{max}, as well as the surface temperature contour for PA11: (a, c, e) in width at [1, 10, 100] mm/min, (b, d, f) in thickness at [1, 10, 100] mm/min.

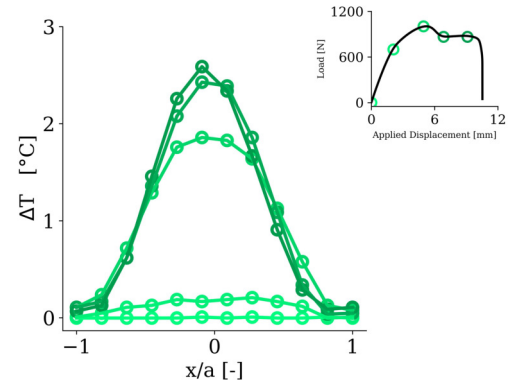

(a) PA11, width, 1 mm/min

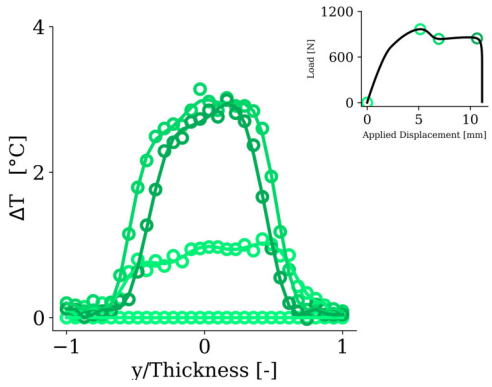

(b) PA11, thickness, 1 mm/min

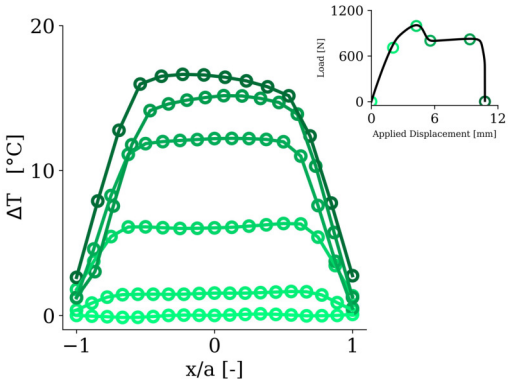

(c) PA11, width, 10 mm/min

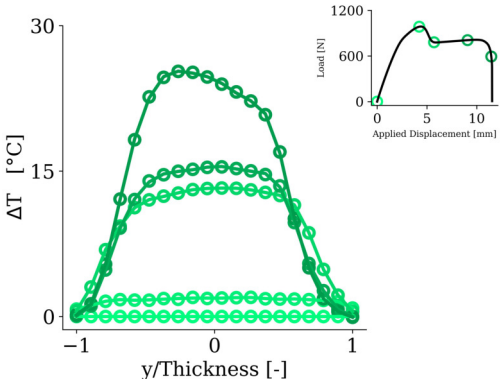

(d) PA11, thickness, 10 mm/min

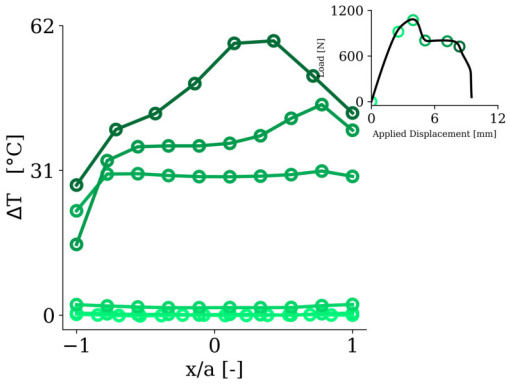

(e) PA11, width, 100 mm/min

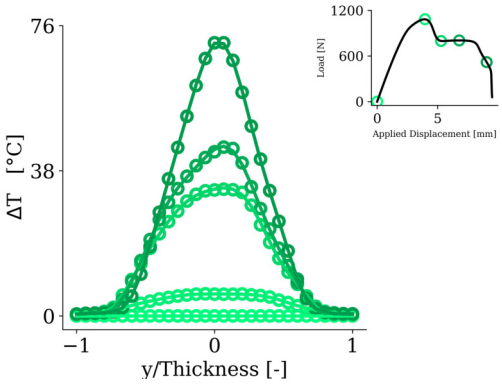

(f) PA11, thickness, 100 mm/min

Figure 15: Temperature profile at the notch root for: PA11 in width (a, b, c), PA11 in thickness (d, e, f) and PE in width (g).

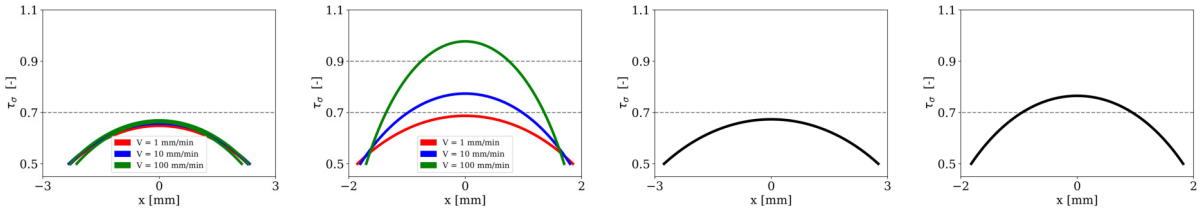

(a) PA11, τ_σ at Fmax **(b)** PA11, τ_σ at Fs **(c)** PE, τ_σ at Fmax **(d)** PE, τ_σ at Fs

Figure 16: The τ_σ distribution along sample width at the minimum section for: (a) PA11 at Fmax, (b) PA11 at Fs, (c) PE at Fmax, (d) PE at Fs

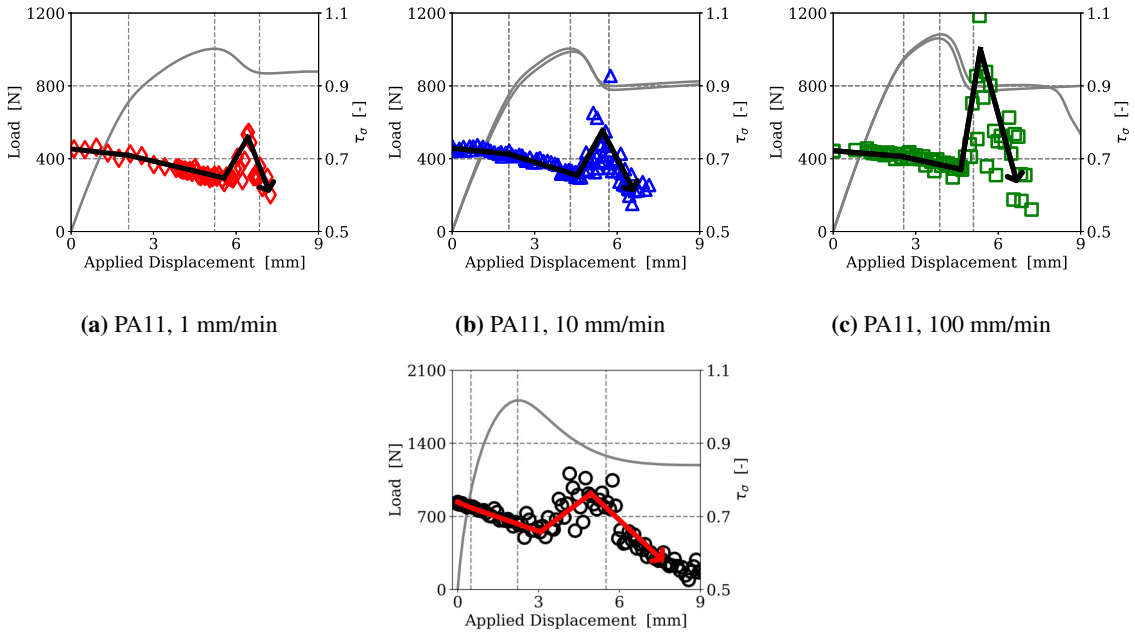

(a) PA11, 1 mm/min **(b)** PA11, 10 mm/min **(c)** PA11, 100 mm/min

(d) PE, 12 mm/min

Figure 17: The evolution of the stress triaxiality ratio τ_σ at sample center for: (a, b, c) PA11 at three different cross-head speeds, (d) PE at 12 mm/min.

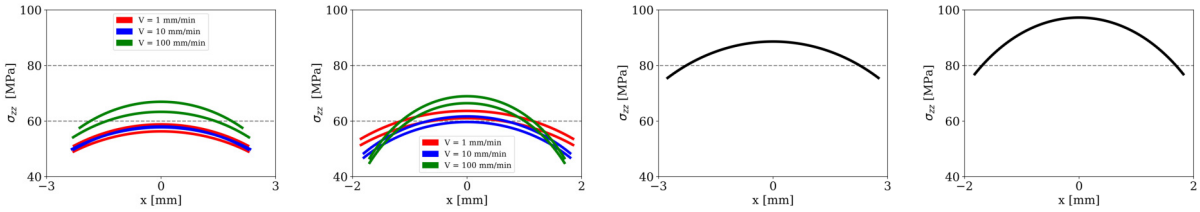

(a) PA11, Fmax **(b)** PA11, Fs **(c)** PE, Fmax **(d)** PE, Fs

Figure 18: The spatial distribution of σ_{zz} along the minimum width for: (a) PA11 at Fmax, (b) PA11 at Fs, (c) PE at Fmax, (d) PE at Fs.

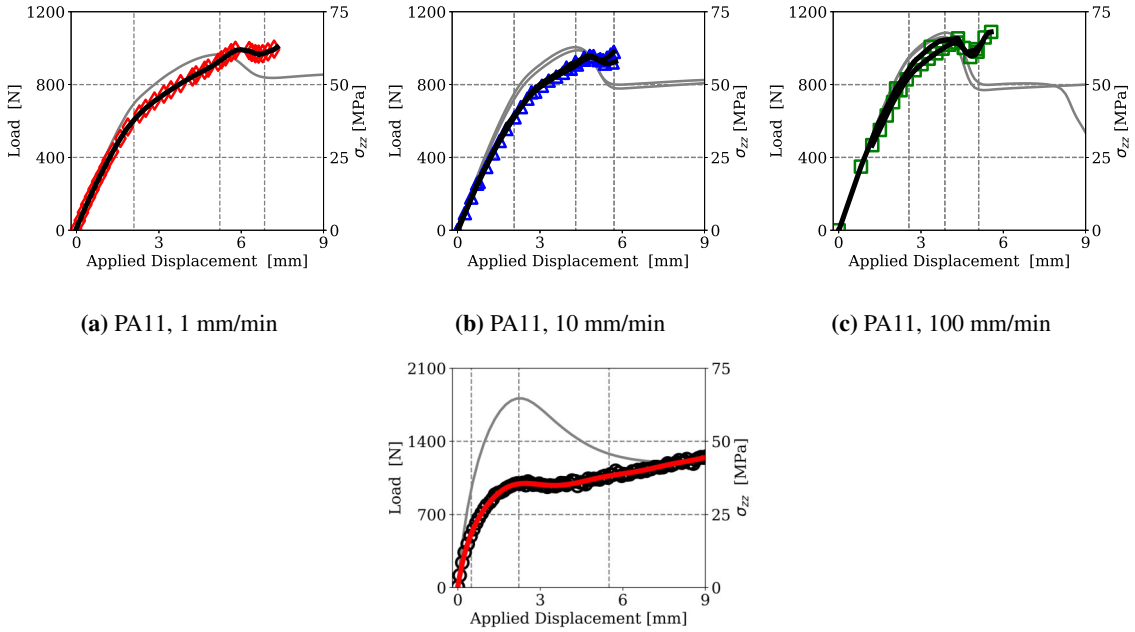

(a) PA11, 1 mm/min

(b) PA11, 10 mm/min

(c) PA11, 100 mm/min

(d) PE, 12 mm/min

Figure 19: The evolution of the maximum principal stress σ_{zz} at sample center for: (a, b, c) PA11 at three different cross-head speeds, (d) PE at 12 mm/min.

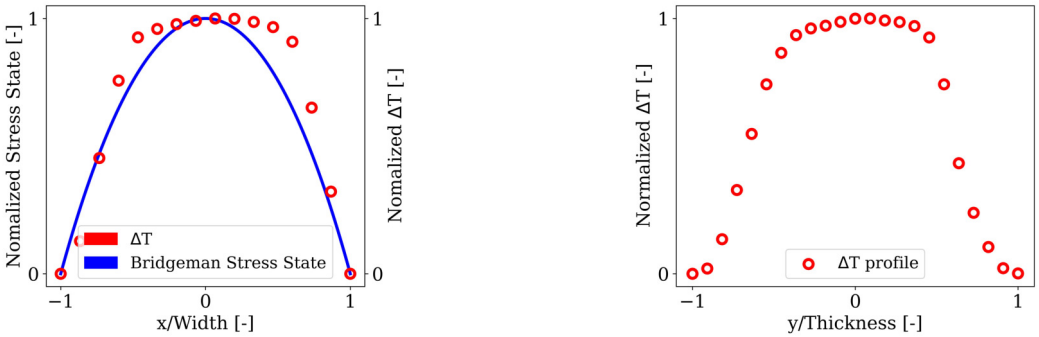

(a)

(b)

Figure 20: Red curves: ΔT profile in width (a), in thickness (b), Blue curve: Bridgman stress state profile in width (a)

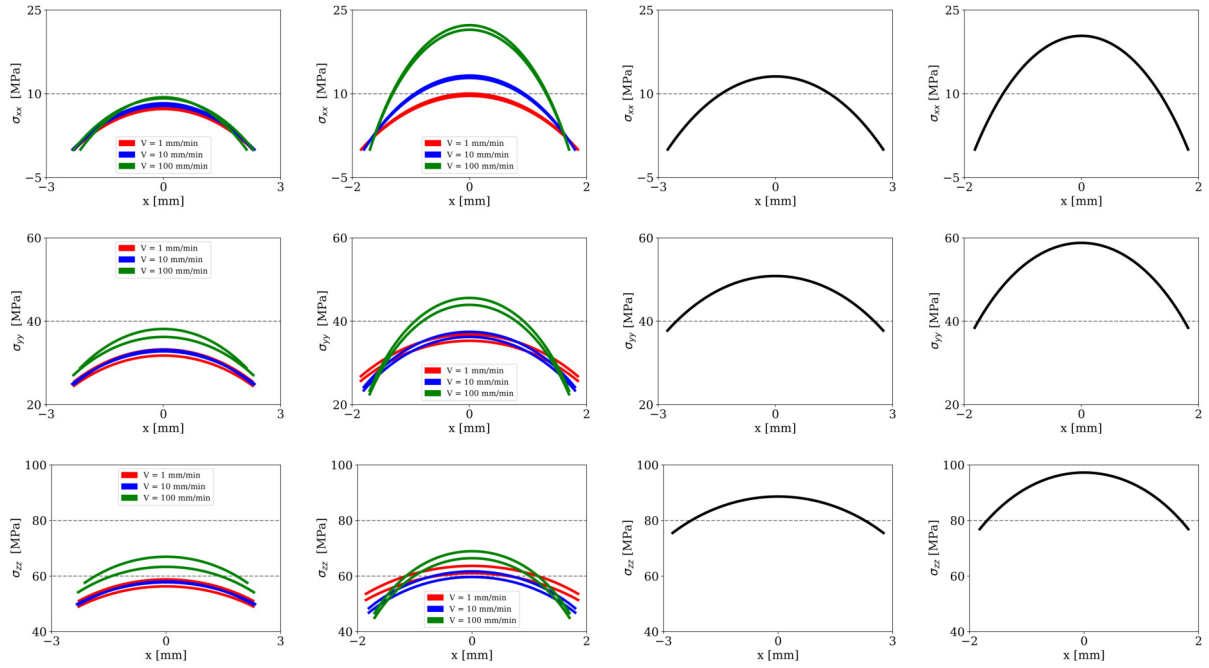

(a) PA11, Fmax **(b)** PA11, Fs **(c)** PE, Fmax **(d)** PE, Fs

Figure 21: The distribution of principal stresses σ_{xx}, σ_{yy}, σ_{zz} along sample width at peak load Fmax and at the end of the load-softening Fs. The three rows display respectively the distribution of σ_{xx}, σ_{yy}, σ_{zz}, from the top to bottom. The four columns display respectively the stress evolution: (a) at Fmax for PA11, (b) at Fs for PA11, (c) at Fmax for PE, (d) at Fs for PE.

Appendix

Principal stresses distribution The following figures display the principal stresses distribution along the sample width at peak load (Fmax) and the end of the load-softenng (Fs) for PA11 and PE. The three rows display respectively the distribution of σ_{xx}, σ_{yy}, σ_{zz}, from the top to bottom. The four columns display respectively the stress evolution: at Fmax for PA11, at Fs for PA11, at Fmax for PE, at Fs for PE, from the left to right. From theses figures, the principal stresses are less sensitive to the lower cross-head speed (less than 10 mm/min), the values are, however, highest at 100 mm/min. The maximum σ_{xx} and σ_{yy} at mid-width is higher at the end of the load-softening than at peak load. The stress level is generally higher for PE than for PA11 whatever the cross-head speed. Despite of materials, the σ_{zz} is always the highest and σ_{xx} the lowest among three principal stresses.

Principal stresses evolution These following figures present the evolution of the three principal stresses σ_{xx}, σ_{yy}, σ_{zz} for PA11 and PE. The first three columns presents each the results of PA11

at one cross-head speed, from left to right, [1, 10, 100] mm/min respectively, the last column is the results for PE at 12 mm/min. Each row presents, from the top to bottom, the evolution of σ_{xx}, σ_{yy}, σ_{zz}. The evolution of σ_{xx} seems to have the same trends regardless of the cross-head speed : 1) begins by a steady growth at the linear stage, 2) then attains quasi-constant during the nonlinear stage, 3) followed by a significant increase during the load-softening, 4) finally finishes by a dramatic drop at the load-plateau stage. Concerning to σ_{yy}, the principal stress seems keeping increasing at the cross-head speed below 10 mm/min, while a stress drop is presented at 100 mm/min. For σ_{zz}, an unignorable stress decrease is observed during the load-softening period whose extent depends strongly on the cross-head speed. The profiles of the evolution of three principal stresses of PE at 12 mm/min seems close to the ones of PA11 at 10 mm/min: both have a small stress drop during the load-softening. The scale of the principal stresses is: σ_{zz} ¿ σ_{yy} ¿ σ_{xx}.

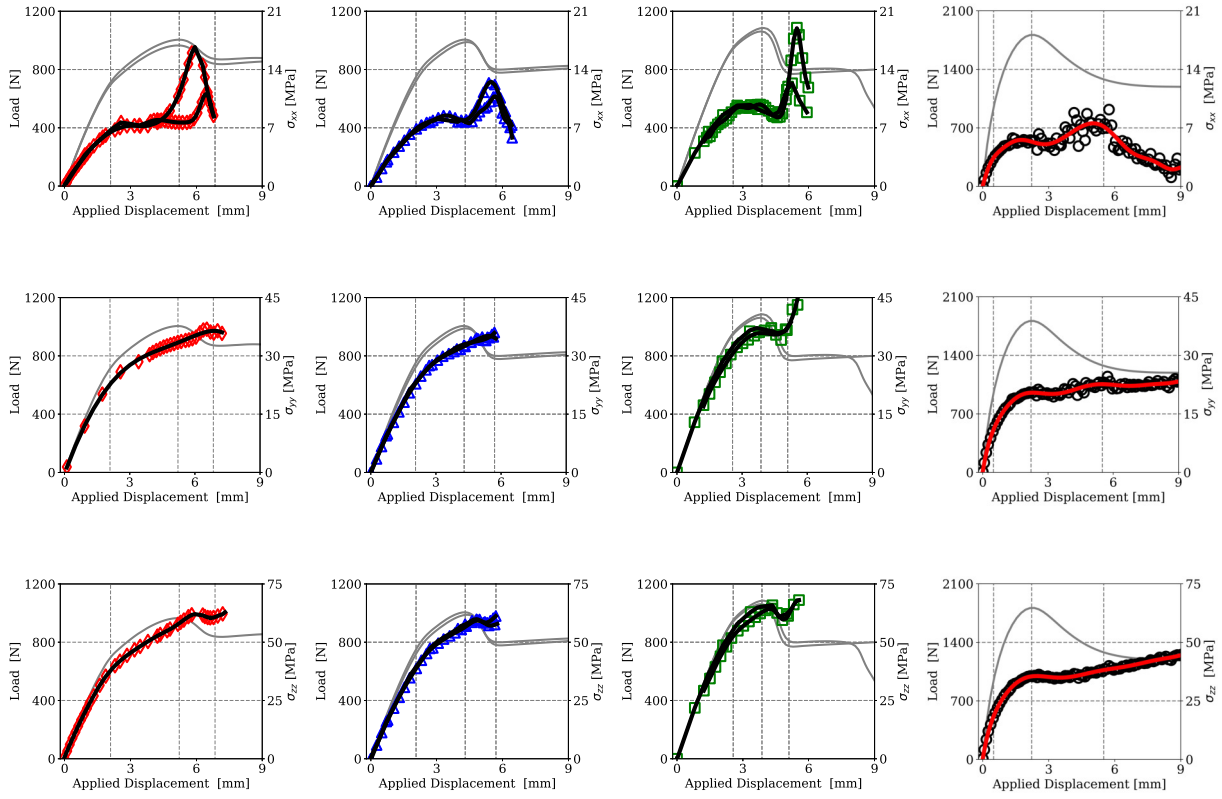

(a) PA11, 1 mm/min **(b)** PA11, 10 mm/min **(c)** PA11, 100 mm/min **(d)** PE, 12 mm/min

Figure 22: The principal stresses evolution at sample center for PA11 an PE, the first row displays the σ_{xx}, the second row is the σ_{yy}, the third row is the σ_{zz}. Figures in columns (a,b,c) are stress evolution for PA11 at three cross-head speeds [1, 10, 100] mm/min, figures in column (d) are the stress evolution of PE at 12 mm/min.

8 References

[1] H. M. Laun. Description of the non-linear shear behaviour of a low density polyethylene melt by means of an experimentally determined strain dependent memory function. *Rheologica Acta*, 17(1):1–15, 1978. doi:10.1007/BF01567859.

[2] A. D. Mulliken and M. C. Boyce. Mechanics of the rate-dependent elastic–plastic deformation of glassy polymers from low to high strain rates. *International Journal of Solids and Structures*, 43(5):1331–1356, 2006. doi:10.1016/j.ijsolstr.2005.04.016.

[3] C. G'sell and J. J. Jonas. Determination of the plastic behaviour of solid polymers at constant true strain rate. *Journal of Materials Science*, 14(3):583–591, 1979. doi:10.1007/BF00772717.

[4] S.M. Walley. A study of the rapid deformation behaviour of a range of polymers. *Philosophical Transactions of the Royal Society of London. Series A, Mathematical and Physical Sciences*, 328(1597):1–33, 1989. doi:10.1098/rsta.1989.0020.

[5] C. Bauwens-Crowet. The compression yield behaviour of polymethyl methacrylate over a wide range of temperatures and strain-rates. *Journal of Materials Science*, 8(7):968–979, 1973. doi:10.1007/BF00756628.

[6] G. I. Taylor and H. Quinney. The latent energy remaining in a metal after cold working. *Proceedings of the Royal Society of London. Series A, Containing Papers of a Mathematical and Physical Character*, 143(849):307–326, 1934. doi:10.1098/rspa.1934.0004.

[7] G. W. Adams and R. J. Farris. Latent energy of deformation of bisphenol a polycarbonate. *Journal of Polymer Science Part B: Polymer Physics*, 26(2):433–445, 1988. doi:10.1002/polb.1988.090260216.

[8] S. N. Rudnev, O. B. Salamatina, V. V. Voenniy, and E. F. Oleynik. Plastic deformation kinetics for glassy polymers and blends. *Colloid and Polymer Science*, 269(5):460–468, 1991. doi:10.1007/BF00655883.

[9] D. Rittel. On the conversion of plastic work to heat during high strain rate deformation of glassy polymers. *Mechanics of Materials*, 31(2):131–139, 1999. doi:10.1016/S0167-6636(98)00063-5.

[10] J. J. Mason, A. J. Rosakis, and G. Ravichandran. On the strain and strain rate dependence of the fraction of plastic work converted to heat: an experimental study using high speed infrared detectors and the kolsky bar. *Mechanics of Materials*, 17(2):135–145, 1994. doi:10.1016/0167-6636(94)90054-X.

[11] D. Rittel. Experimental investigation of transient thermoplastic effects in dynamic fracture. *International Journal of Solids and Structures*, 37(21):2901–2913, 1999. doi:10.1016/S0020-7683(99)00043-8.

[12] V. Bellenger, A. Tcharkhtchi, and Ph. Castaing. Thermal and mechanical fatigue of a PA66/glass fibers composite material. *International Journal of Fatigue*, 28(10):1348–1352, 2006. doi:10.1016/j.ijfatigue.2006.02.031.

[13] S. C. Chou, K. D. Robertson, and J. H. Rainey. The effect of strain rate and heat developed during deformation on the stress-strain curve of plastics. *Experimental Mechanics*, 13(10):422–432, 1973. doi:10.1007/BF02324886.

[14] S.B. Ratner, V.I. Korobov, and S.G. Agamalyan. Mechanical and the thermal fracture plastics under cyclic strains. *Fiziko-Khimicheskaya Mekhanika Materialov*, 5(1):88–93, 1969. doi:10.1007/bf00721313.

[15] M. C. Boyce, D. M. Parks, and A. S. Argon. Large inelastic deformation of glassy polymers. part II: numerical simulation of hydrostatic extrusion. *Mechanics of Materials*, 7(1):35–47, 2021. doi:10.1016/0167-6636(88)90004-X.

[16] E. M. Arruda, M. C. Boyce, and R. Jayachandran. Effects of strain rate, temperature and thermomechanical coupling on the finite strain deformation of glassy polymers. *Mechanics of Materials*, 19(2):193–212, 1995. doi:10.1016/0167-6636(94)00034-E.

[17] A. Lion. On the large deformation behavior of reinforced rubber at different temperatures. *Journal of the Mechanics and Physics of Solids*, 45(11):1805 – 1834, 1997. doi:10.1016/S0022-5096(97)00028-8.

[18] D. Rittel. An investigation of the heat generated during cyclic loading oftwo glassy polymers. part i: Experimental. *Mechanics of Materials*, 32(131), 2000. doi:10.1016/S0167-6636(99)00051-4.

[19] L. Laiarinandrasana, J. Besson, M. Lafarge, and G. Hochstetter. Temperature dependent mechanical behaviour of PVDF: Experiments and numerical modelling. *International Journal of Plasticity*, 25(7):1301–1324, 2009. doi:10.1016/j.ijplas.2008.09.008.

[20] S. Basu and E. Van der Giessen. A thermo-mechanical study of mode i,small-scale yielding crack-tip fieldsin glassy polymers. *International Journal of Plasticity*, 18(10):1395 – 1423, 2001. doi:10.1016/S0749-6419(02)00009-8.

[21] F. Shen, G. Kang, Y. C. Lam, Y. Liu, and K. Zhou. Thermo-elastic-viscoplastic-damage model for self-heating and mechanical behavior of thermoplastic polymers. *International Journal of Plasticity*, 121:227–243, 2019. doi:10.1016/j.ijplas.2019.06.003.

[22] Maximilian Ly, Kamran A.Kan, and Anastasia Muliana. Modeling self-heating under cyclic loading in fiber-reinforced polymer composites. *Journal of Materials Engineering and Performance*, 2020. doi:10.1007/s11665-020-04663-7.

[23] C. Ovalle, G. Boisot, and L. Laiarinandrasana. Effects of stress triaxiality ratio on the heat build-up of polyamide 11 under loading. *Mechanics of Materials*, 145:103375, 2020. doi:10.1016/j.mechmat.2020.103375.

[24] M. Challier, J. Besson, L. Laiarinandrasana, and R. Piques. Damage and fracture of polyvinylidene fluoride (PVDF) at 20c: Experiments and modelling. *Engineering Fracture Mechanics*, 73(1):79–90, 2006. doi:10.1016/j.engfracmech.2005.06.007.

[25] S. Castagnet and Y. Deburck. Relative influence of microstructure and macroscopic triaxiality on cavitation damage in a semi-crystalline polymer. *Materials Science and Engineering: A*, 448(1):56–66, 2007. doi:10.1016/j.msea.2006.11.100.

[26] G. Boisot, L. Laiarinandrasana, J. Besson, C. Fond, and G. Hochstetter. Experimental investigations and modeling of volume change induced by void growth in polyamide 11. *International Journal of Solids and Structures*, 48:2642–2654, 2011. doi:10.1016/j.ijsolstr.2011.05.016.

[27] L. Laiarinandrasana, T. F. Morgeneyer, H. Proudhon, F. N'guyen, and E. Maire. Effect of multiaxial stress state on morphology and spatial distribution of voids in deformed semicrystalline polymer assessed by x-ray tomography. *Macromolecules*, 45(11):4658–4668, 2012. doi:10.1021/ma3005247.

[28] Bridgman P.W. The stress distribution at the neck of a tension specimen. In *Twenty-fifth Annual Convention of the Society*, 1943. doi:10.1299/jsme1958.9.637.

[29] C. A Schneider, W. W Rasband, and K. W Eliceiri. NIH image to ImageJ: 25 years of image analysis. *Nature Methods*, 9(7):671–675, 2012. doi:10.1038/nmeth.2089.

[30] P.A. Poulet, G. Hochstetter, A. King, H. Proudhon, S. Joannès, and L. Laiarinandrasana. Observations by in-situ x-ray synchrotron computed tomography of the microstructural evolution of semi-crystalline polyamide 11 during deformation. *Polymer Testing*, 56:245–260, 2016. doi:10.1016/j.polymertesting.2016.10.023.

[31] S. N. Olufsen, A. H. Clausen, D. W. Breiby, and O. S. Hopperstad. X-ray computed tomography investigation of dilation of mineral-filled PVC under monotonic loading. *Mechanics of Materials*, 142:103296, 2020. doi:10.1016/j.mechmat.2019.103296.

[32] Eric N. Brown, Philip J. Rae, and E. Bruce Orler. The influence of temperature and strain rate on the constitutive and damage responses of polychlorotrifluoroethylene (PCTFE, kel-f 81). *Polymer*, 47(21):7506–7518, 2006. doi:10.1016/j.polymer.2006.08.032.

[33] Shahzad Fateh A. and J. Fan. Elastic-viscoplastic constitutive model for capturing the mechanical response of polymer composite at various strain rates. *Journal of Materials Science & Technology*, 57:12–17, 2020. doi:10.1016/j.jmst.2020.05.013.

[34] R. Steinberger, T.I. Valadas Leitao, E Ladstatter, G. Pinter, W Billinger, and R.W. Lang. Infrared thermographic techniques for non-destructive damage characterization of carbon fibre reinforced polymers during tensile fatigue testing. *International Journal of Fatigue*, 28:1340–1347, 2006. doi:10.1016/j.ijfatigue.2006.02.036.